coatings

MDPI

Article

Effects of Incorporating TiO_2 Aggregates on the Growth, Anticorrosion, and Antibacterial Properties of Electrodeposited Multifunctional Coatings Based on Sn-Ni Materials

Hanna Pianka [1], Valeria P. Boufal [1], Olga Alisiyonok [1], Maxim Vlasov [2], Alexander Chernik [1], Yanpeng Xue [3] and Abdelhafed Taleb [4,*]

[1] Department of Chemistry, Technology of Electrochemical Production and Materials of Electronic Engineering, Belarusian State Technological University, 13a Sverdlova St., 220006 Minsk, Belarus; hanna.pianka@mail.ru (H.P.); leraboufal85@gmail.com (V.P.B.); alisiyonak@belstu.by (O.A.); alexachernik@gmail.com (A.C.)
[2] Institute of High Temperature Electrochemistry, Ural Branch of the Russian Academy of Sciences, Akademicheskaya St., 20, 620066 Yekaterinburg, Russia; m_vlasov@ihte.ru
[3] National Center for Materials Service Safety, University of Science and Technology Beijing, Xueyuan Road 30, Beijing 100083, China; yanpengxue@ustb.edu.cn
[4] Chemistry Department, Sorbonne Université, 4 Place Jussieu, 75231 Paris, France
* Correspondence: abdelhafed.taleb@sorbonne-universite.fr; Tel.: +33-1-85-78-41-97

Abstract: Multifunctional coatings based on Sn-Ni materials with and without titanium oxide nanoparticles (TiO_2NPs) incorporation were prepared using the electrochemical deposition technique at 70 °C. TiO_2NPs were dispersed in the electrolyte bath, and their influence on the surface texture, crystalline phase, and properties was investigated. Various techniques such as X-ray diffraction (XRD), scanning electron microscopy (SEM), and energy dispersive X-ray microanalysis (EDX) were used to characterize the prepared coatings. The formation mechanism of the deposited coatings has been demonstrated to be consistent with the electrochemical behavior of instantaneous growth, and the three-dimensional growth is controlled by diffusion phenomena. The anticorrosion effectiveness of the coatings was assessed using potentiodynamic polarization curves and electrochemical impedance spectroscopy in an artificial sweat medium, while the bactericidal activity of the composite coatings (the ability to induce cell death) was evaluated in accordance with the ISO 27447:2019 test. The influence of TiO_2NPs at a low concentration of 1 g/L on the composition, structure, and properties of the deposited coatings was demonstrated. Particular attention was paid to the relationship between the anticorrosive and bactericidal properties of the coatings and their structure composition and wetting properties. The synergistic effect of chemical composition and surface-wetting properties has been demonstrated to enhance the anticorrosive and bactericidal properties of the prepared coatings.

Keywords: multifunctional coating; anticorrosion; antibacterial; Sn-Ni thin films; TiO_2 nanoparticles

Citation: Pianka, H.; Boufal, V.P.; Alisiyonok, O.; Vlasov, M.; Chernik, A.; Xue, Y.; Taleb, A. Effects of Incorporating TiO_2 Aggregates on the Growth, Anticorrosion, and Antibacterial Properties of Electrodeposited Multifunctional Coatings Based on Sn-Ni Materials. *Coatings* **2024**, *14*, 1344. https://doi.org/10.3390/coatings14111344

Academic Editor: Daniela Predoi

Received: 31 August 2024
Revised: 10 October 2024
Accepted: 17 October 2024
Published: 22 October 2024

1. Introduction

In recent years, there has been a growing demand for multifunctional coatings that combine physical, biological, chemical, and mechanical properties, such as increased hardness, decorative appearance, corrosion resistance, hydrophobicity, and antibacterial properties. Indeed, the changing conditions in which coatings are used require them to be multifunctional to meet the challenges and demands of their environment. Various approaches have been developed to produce coatings with numerous properties, making them multifunctional. Among these approaches, those that combine different chemical elements and controlled nanostructuring of the surface have proven to be very effective in producing multifunctional coatings. Alloys produced by electrochemical deposition have demonstrated their ability to exhibit multiple properties, which can lead to the multifunctional nature of certain coatings and their widespread use in industry.

Metallic coatings have evolved considerably in recent centuries, from single-layer coatings to multi-layer-gradient and micro-stack coatings and from alloy coatings to composite coatings. The most common alloys used in coatings are nickel-based—notably nickel–tin—which offer a wide range of properties such as corrosion, wear, and abrasion resistance. To date, protective metals and alloys such as Zn [1], Ni-based alloys [2], Al-based alloys [3], Ti [4], Hf [5], Cr [6], and Cu [7] have been investigated for various applications, particularly for metals that are prone to corrosion.

The combination of chemical elements in an alloy represents an effective strategy for creating synergies between the properties of these elements. This approach can result in the enhancement of existing properties or the emergence of new ones [8–10]. The study and development of alloys of different metals, as well as their shaping into layers, represent a significant area of research within the field of materials science.

Coatings with anticorrosive, superhydrophobic, and antibacterial properties [11–14] are currently in demand for certain surfaces that require constant disinfection, such as door handles, handrails, lift buttons, etc. The antibacterial properties and aesthetic appeal of Cu-based electrochemical coatings have been extensively documented in the scientific literature [15–18]. TiO_2 is another material that has been extensively documented in the scientific literature for its photocatalytic and antibacterial properties in metal coatings [19–21]. The synthesis method and preparation conditions often determine many of the characteristics and properties of TiO_2 nanoparticles, such as size, morphology, crystalline phase, degree of agglomeration, etc. [22–25]. TiO_2 has been used as an inert phase in composite coatings based on Cu [15,16], Zn [26,27], Ni [28–32], and alloys [33–37] to impart photocatalytic and antibacterial properties. The impact of ultrasonic treatment on the electrodeposition of Cu-Sn-TiO_2NP nanocomposite coatings with enhanced antibacterial properties has been the subject of extensive research in the literature [15]. The effect of ultrasonic treatment and current loading on microstructure, quantitative and qualitative composition, distribution of TiO_2NP aggregates, and antibacterial properties against *E. coli* bacteria was demonstrated. Furthermore, a comparative study was conducted to examine the impact of mechanical agitation and ultrasound on the characteristics of the nanocomposite coatings produced.

Electrochemically produced Sn-Ni-based alloy coatings are widely used in metal finishing and microelectronics [38–49]. They prevent allergic skin reactions and corrosion in artificial environments [43] and can replace nickel electroplating on the skin of clothing fasteners. They can also replace chromium in the decorative and lighting industries [40]. This alloy combines physical and chemical properties that allow it to be widely used in industry. These include increased corrosion resistance, improved hardness, high wear resistance, and many other properties [38–49]. Various electrolytes have been used to deposit Sn-Ni alloys, including fluoride–chloride [34,36], pyrophosphate [39,41], sulphuric acid [42], glyconat [42], and others. Various studies have reported the influence of the kinetic parameters of Sn-Ni alloy deposition on its physicochemical and mechanical properties [40–49] as well as on composite coatings with TiO_2 NPs of different phase compositions [33–36]. Visible and photoactive Sn-Ni-TiO_2NP coatings incorporating carbon-doped particles and N- and S-doped TiO_2NPs (N, S-TiO_2NPs) have been reported in the literature [34]. It has been reported that the optimum parameters for obtaining the best co-deposition rates of carbon and doped TiO_2NPs are a low current density of 0.01 A/cm^2 and a concentration of 30 g/L under DC conditions. The highest co-deposition percentage of 3.25 wt% was obtained in the case of incorporation of N, S-TiO_2NPs. TiO_2 NPs synthesized by direct oxidation of titanium are reported in the literature [35,36] to have yielded a mixture of two TiO_2 polymorphs, anatase and rutile, with particle sizes between 30 and 50 nm. The effect of the TiO_2NP aggregate content on the physicochemical and biocidal properties of Sn-Ni coatings has been demonstrated [36].

The present work aimed to study the kinetics of electrochemical deposition of Sn-Ni-TiO_2NP composite coatings, as well as the effect of the incorporation of TiO_2NPs synthesized by the hydrothermal method on their properties. The mechanism of coating formation was also investigated. Furthermore, the corrosion resistance and antibacterial

properties of Sn-Ni-TiO_2NP coatings were investigated in an artificial sweat environment. The relationships between the properties of the coatings and their structure, composition, and surface roughness were demonstrated. These results allow us to evaluate the use of these coatings for public applications such as door handles, turnstiles, lift buttons, etc.

2. Materials and Methods

The Sn-Ni alloy coating was deposited using a fluoride–chloride electrolyte, with the ionic strength of the solution compensated by sodium chloride. The compositions of the solutions used are provided in Table 1.

Table 1. Composition of different electrolytes used for coatings deposition: Electrolyte 1 for Ni-Sn coating deposition, Electrolyte 2 for Sn coating deposition, and Electrolyte 3 for Ni coating deposition.

Component	Concentration, mol/L		
	Electrolyte 1	Electrolyte 2	Electrolyte 3
$SnCl_2 \cdot 2H_2O$	0.22 ± 0.02	0.22 ± 0.02	–
$NiCl_2 \cdot 6H_2O$	1.05 ± 0.02	–	1.05 ± 0.02
NH_4F	1.35 ± 0.14	1.35 ± 0.05	1.35 ± 0.05
NaCl	–	3.19 ± 0.03	0.67 ± 0.03

Electrolytes were prepared using double-distilled water and analytical grade $NiCl_2 \cdot 6H_2O$, $SnCl_2 \cdot 2H_2$.

The reagents were purchased from Belreachim, Minsk, Belarus. NH_4F, NaCl, and HCl compounds were also purchased from Belreachim. After mixing all the electrolyte components, the pH of the electrolyte was adjusted with 0.1 M HCl, and 1 g/L of TiO_2NPs—synthesized according to the procedure described in [25]—was added to the electrolyte composition. The electrolysis was carried out at a temperature of 70 °C, pH of 3, a current density of 0.01 A/cm^2, with continuous stirring using a magnetic stirrer, and the anode material consisted of nickel and tin. The anode was enclosed in fabric sheaths (polypropylene fabric (KS–34) chlorine) to avoid contamination of the electrolyte by sludge. Copper was used as the cathode material.

The kinetics of the coating deposition was studied by chronovoltammetry and chronoamperometry using an Autolab PGSTAT 302N (Ecochemie, The Netherlands) potentiostat and a three-electrode configuration consisting of a saturated silver chloride electrode as the reference electrode and a platinum electrode as the counter-electrode.

The most commonly used model to describe the electrocrystallization process is that of Scharifker and Hills (SH) [35]. This model is used to determine the type of nucleation by analyzing the rising parts of the chronoamperograms before the nuclei diffusion zones overlap. Depending on the slope of these parts of the chronoamperogram, two types of nucleation can be identified: instantaneous and progressive. Instantaneous nucleation corresponds to the situation where all the nucleation sites on the surface are immediately activated by the applied potential. Furthermore, the number of nuclei remains globally unchanged during the growth process.

In the case of progressive nucleation, the number of nuclei increases progressively with deposition time. Equations (1) and (2) describe progressive and instantaneous nucleation, respectively, in the electroplating process [50]:

$$\left(\frac{i}{i_{max}}\right)^2 = \frac{1.9542}{\frac{t}{t_{max}}}\left\{1 - exp\left[-1.2564\frac{t}{t_{max}}\right]\right\}^2 \cdot instanneous \quad (1)$$

$$\left(\frac{i}{i_{max}}\right)^2 = \frac{1.2254}{\frac{t}{t_{max}}}\left\{1 - exp\left[-2.3367\frac{t}{t_{max}}\right]^2\right\}^2 \cdot progressive \quad (2)$$

where i_{max} is the maximum current from a current transient at a corresponding time, denoted by t_{max}.

The phase composition of the coatings was determined by X-ray diffraction (XRD) analysis using a Bruker D8 Advance AXS diffractometer, Ettlingen, Germany. X-ray scanning was performed at a rate of 1° s^{-1} using CuKα radiation. The position of the maxima of the analyzed peaks was measured with an accuracy of ±0.05°.

The Raman spectra were measured at room temperature using a U1000 Raman microscope-spectrometer (Renishaw, Wotton-under-Edge, UK), and laser radiation with a wavelength of 532 nm (power: 5 mW on the sample). Registration was carried out with a spectral resolution of 1 cm^{-1}.

The prepared coatings' surface morphology was studied by scanning electron microscopy (SEM) using a JEOL JSM-5610 LV microscope, Tokyo, Japan, while their elemental composition was determined by energy dispersive X-ray (EDX) microanalysis using a JED-2201 EDX (JEOL, Tokyo, Japan).

Corrosion tests were carried out in an artificial sweat medium, the composition of which is shown in Table 2.

Table 2. The composition of artificial sweat electrolyte.

Compounds	Sodium Chloride (NaCl)	Ammonium Chloride (NH_4Cl)	Urea ($(NH_2)_2CO$)	Acetic Acid (CH_3COOH)	L-Lactic Acid ($C_3H_6O_3$)
Concentration, g/L	20.0	17.5	5.0	2.5	15.0

Polarization curves were recorded at a sweep rate of 1 mV/s, 20 min after the working electrode was immersed in the artificial sweat solution to establish a steady-state potential. Corrosion currents were calculated from the intersection of the straight Tafel sections of the cathode and anode curves. Impedance spectra were recorded in the frequency range from 10 kHz to 0.01 Hz with an AC voltage amplitude of 10 mV. The impedance frequency spectra were recorded 20 min after the sample was kept in the test solution. The data obtained were processed using Nova 2.1 and ZView 3.2c software.

Test cultures of the health indicators bacteria *Escherichia coli* (ATCC 8739) and *Staphylococcus aureus* (ATCC 6538) were used to assess the antibacterial properties of the coatings. The antibacterial tests of the composite coatings were conducted according to the standard test method ISO 27447:2019 [51] described in the literature [35]. The evaluation of the bactericidal activity of the composite coatings in terms of their ability to induce cell death was assessed using the reduction factor (RF), which was determined using the following Equation (3):

$$FR = \log(K_1/K_2) \quad (3)$$

where K_1 is the concentration of viable cells in the nutrient medium with the coating examined without UV irradiation (CFU/cm^3); K_2 is the concentration of viable cells in the nutrient medium with the coating examined after UV irradiation (CFU/cm^3).

3. Results and Discussion

The synthesis and formation mechanism of TiO_2NP aggregates has been described in previous works [25]. In the present work, the hydrothermal synthesis temperature was set at 170 °C, and at the end of the synthesis, washing, and annealing processes, a white powder was obtained. The FEGSEM characterization of the TiO_2NP aggregate powders shows a morphology in the form of porous spherical aggregates of several particles (insert Figure 1a). The size of the aggregates varies from 50 to 200 nm (Figure 1).

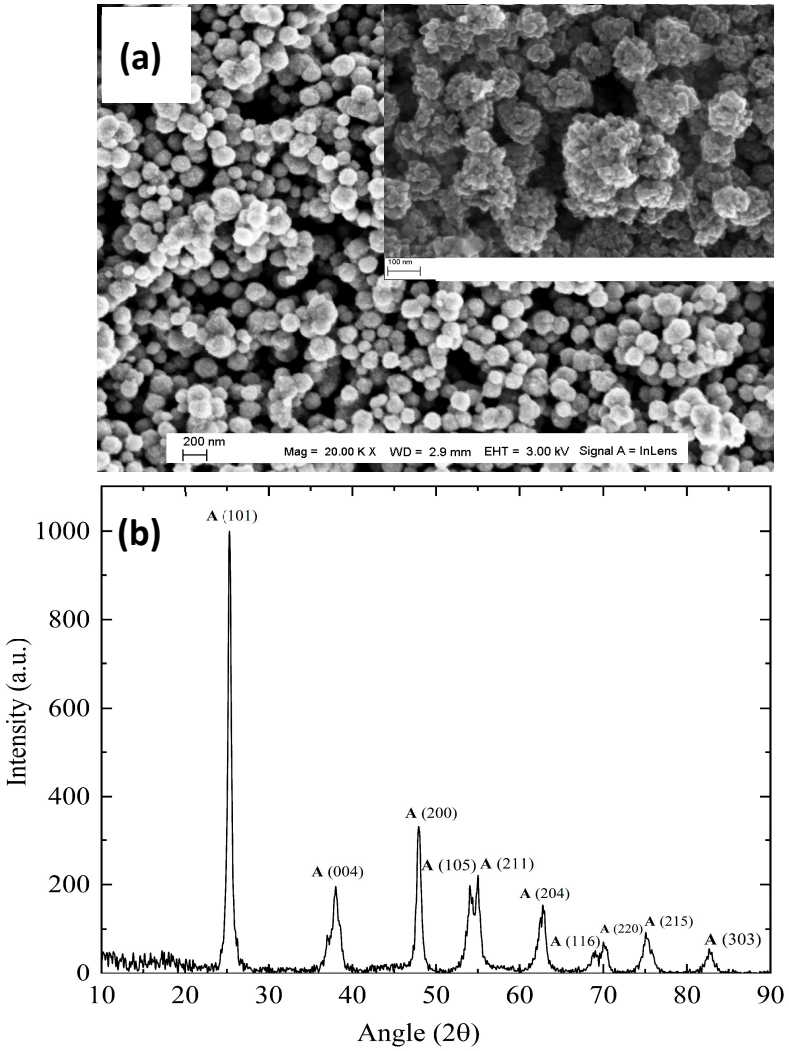

Figure 1. (**a**) FEGSEM images of TiO_2 aggregates obtained at synthesis temperatures of 170 °C, insert depicts the corresponding high magnification; (**b**) XRD pattern of TiO_2NP aggregates prepared at synthesis temperatures 170 °C.

The crystal structure and phase of the prepared TiO_2NP aggregate powder were analyzed by X-ray diffraction. The XRD patterns obtained are shown in Figure 1b and revealed a crystal structure with peaks characteristic of the anatase phase of TiO_2NP aggregates (JCPDS No. 89-4921). This indicates that the powder is crystallized and of high purity.

The synthesized TiO_2NP aggregates were added to the fluoride–chloride electrolyte for the deposition of the Sn-Ni alloy as well as Ni and Sn monolayers, at a concentration of 1 g/L, as described in the Materials and Methods Section. To understand the properties of the Sn-Ni alloy coating, a comparison was made with those of the Sn and Ni coatings. The electrochemical properties of the electrodeposited Sn, Ni, and Sn-Ni alloy composite coatings were studied (Figure 2) with and without the addition of TiO_2NP aggregates to the electrolyte. The electrodeposition of Sn from a fluoride–chloride electrolyte with ionic strength compensation using NaCl proceeds toward potentials more negative than −0.44 V and more positive than −0.34 V for Ni. For the Sn-Ni alloy, the cathodic polarization curve shifts toward the more positive potentials by approximately −0.28 V, indicating a depolarization effect. The introduction of TiO_2NP aggregates into the electrolyte has virtually no effect on the evolution of the cathodic polarization curves of the coating deposition processes.

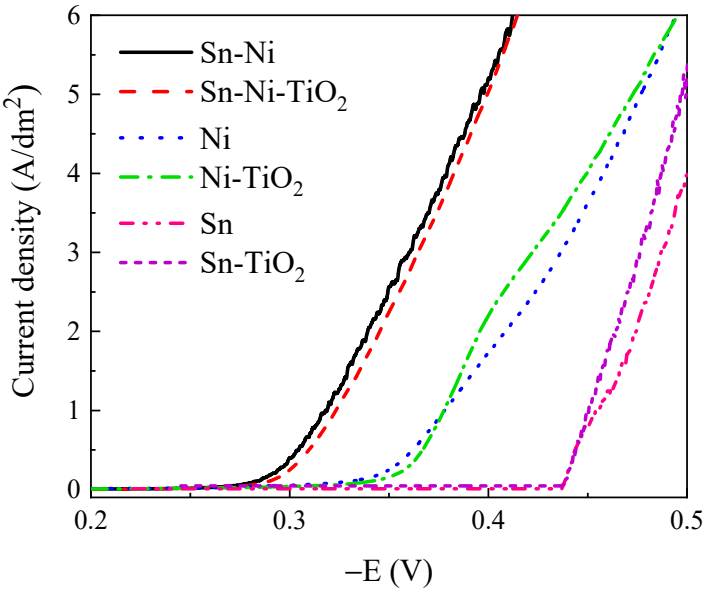

Figure 2. Cathodic polarization curves of Sn, Ni, and Sn-Ni electrodeposition with and without the addition of TiO_2NPs at a temperature of 70 °C as indicated.

To further identify the polarization characteristics accompanying electrochemical deposition reactions, the activation energy for various partial processes has been calculated (Figure 3).

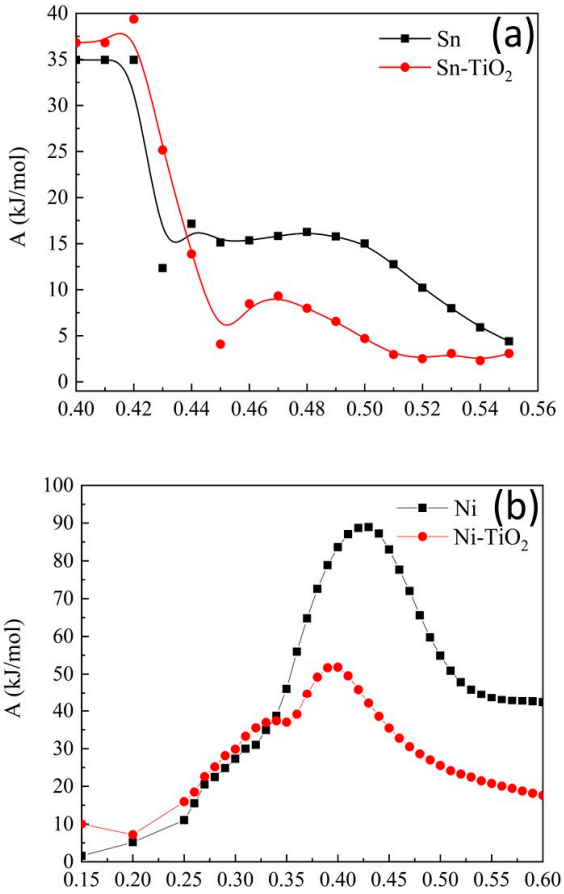

Figure 3. *Cont.*

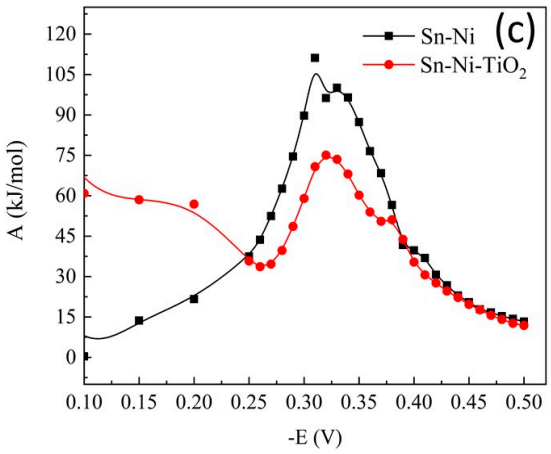

Figure 3. Dependence of the activation energy on the potential of different coatings with and without the addition of TiO_2NPs in the electrolyte as indicated (**a**) Sn and Sn-TiO_2, (**b**) Ni and Ni-TiO_2, and (**c**) Sn-Ni and Sn-Ni-TiO_2.

A comparison of the activation energies of Sn and Sn-TiO_2NPs shows that in the same potential range between −0.4 and −0.44 V, the activation energies decrease uniformly. At potentials between −0.45 and −0.55 V, the variation in the activation energy as a function of potential exhibits a slight shift in the activation energy maximum, which can be attributed to the limitations imposed by the diffusion process in the case of the deposition of Sn and Sn-TiO_2 NPs. This finding is in accordance with the results previously documented in the literature [34]. In the case of the Sn-Ni alloy coatings, a more pronounced activation energy peak is observed at −0.35 V. By comparing the dependence of the activation energy on the deposition potentials of the Sn-Ni alloy and the Sn-Ni-TiO_2NP composite, it can be concluded that the ions are discharged together in the form of intermetallic compounds, and similar results have been reported in the literature [34].

The nucleation mechanism of Sn-Ni electrodeposition was investigated using the chronoamperometry technique and potentiostatic current–time transient curves at varying potentials. The results are presented in Figure 4a. The current demonstrates a peak in the potential range between −230 mV and −410 mV, which can be attributed to the formation and growth of the crystalline nuclei. Subsequently, it exhibits a gradual decrease due to electron transfer, ultimately reaching a plateau at the end stage as a result of the growth of the alloy nuclei. This shows the typical characteristic of a diffusion-controlled electrochemical nucleation process with three-dimensional nucleus growth and can be characterized by Cottrell's equation, which is expressed in Equation (4) as follows [29]:

$$i = \frac{n \cdot F \cdot A \cdot D^{\frac{1}{2}} \cdot c_0}{\pi^{\frac{1}{2}} \cdot t^{\frac{1}{2}}} \quad (4)$$

where i is the current through the electrolyte; n is the number of electrons involved; F is Faraday's constant; A is the working area of the electrode; D is the diffusion coefficient; C_0 is the concentration of the species in the bulk; and, t is the time. The diffusion coefficient is an important kinetic parameter used to estimate the effect of additives on the electrodeposition of Sn-Ni and can be determined from the slope of the chronoamperogram of i versus $t^{1/2}$ according to Cottrell's equation (Equation (4)).

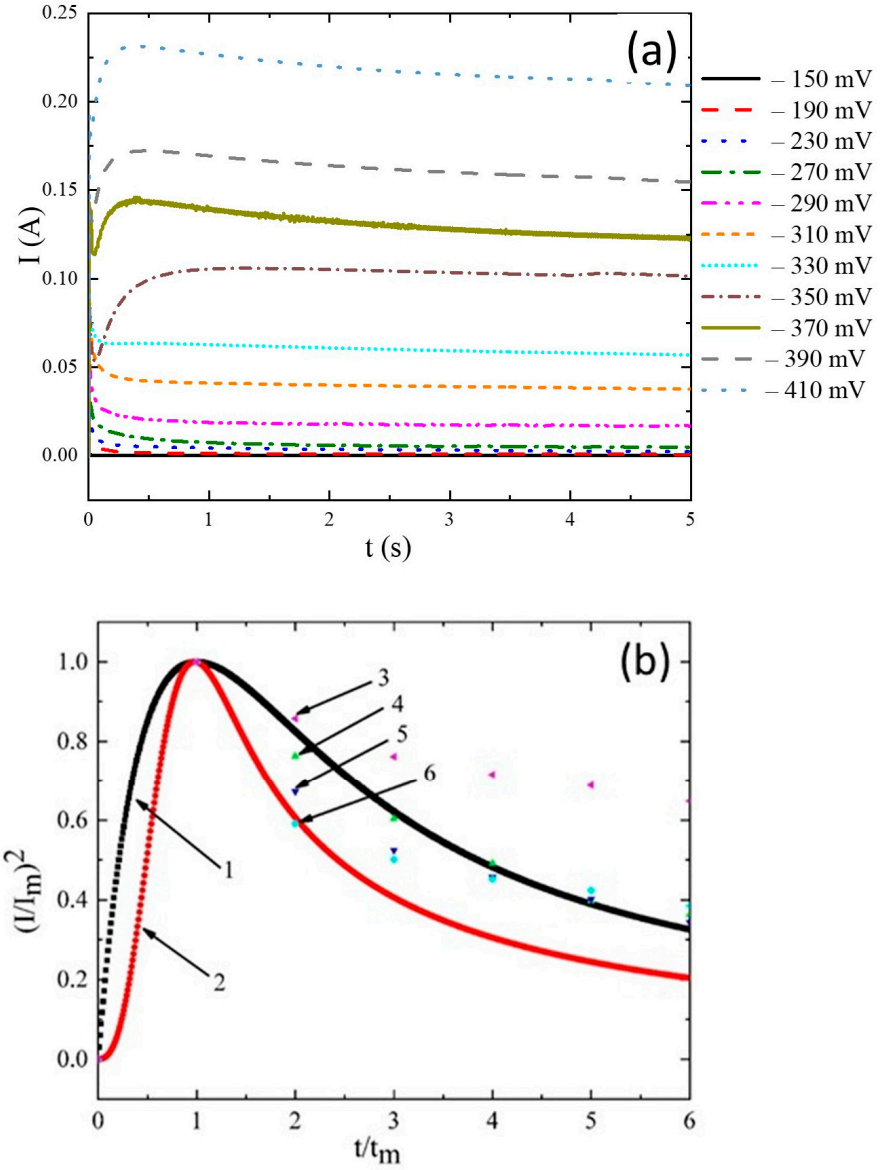

Figure 4. (**a**) Chronoamperograms of the Sn-Ni alloy deposition at various potentials; (**b**) typical current–time transients for the electrodeposition of a Sn-Ni alloy from a fluoride–chloride electrolyte (T = 70 °C) at different applied potentials, V: (3) −0.250; (4) −0.310; (5) −0.320; (6) −0.390. Theoretical representations of the SH models in cases 1—instantaneous nucleation, and 2—progressive nucleation.

It has been observed that as the potential shifts toward more electronegative values down to −410 mV, the time taken to reach the maximum current on the chronoamperograms increases (Figure 4a).

A comparison of some other parameters—such as the maximum value of the transient current (i_m) and the time to reach it (t_m) for the electrodeposited alloy at different applied potentials—is shown in Figure 4b. It can be seen that when the potential is more negative, the value of i_m is higher and the value of t_m is greater. A comparison of the curves obtained at different potentials with the theoretical instantaneous and progressive curves of the SH model is shown in Figure 4b. This comparison shows that the experimental curves are closer to an instantaneous nucleation model; therefore, the electrodeposition of Sn-Ni follows an instantaneous nucleation mechanism and the three-dimensional growth is controlled by the diffusion process [39]. In addition, the deposition potential slightly affects the Sn-Ni nucleation mechanism. However, Figure 4b shows that when $t > t_m$, the experimental curves deviate from the theoretical instantaneous nucleation behavior due to proton reduction

during Sn-Ni electrodeposition. This can occur during the electrodeposition of metal ions in aqueous solutions, as observed in previous work [41].

The SEM and EDX characterizations in Figure 5 show that within 2 s of electrolysis at a potential of 0.32 V, the nuclei begin to coalesce to form a continuous film, while the Ni content of the alloy formed has almost twice the Sn content. This could be an indication of the predominance of Ni deposition in the early stages of electrolysis.

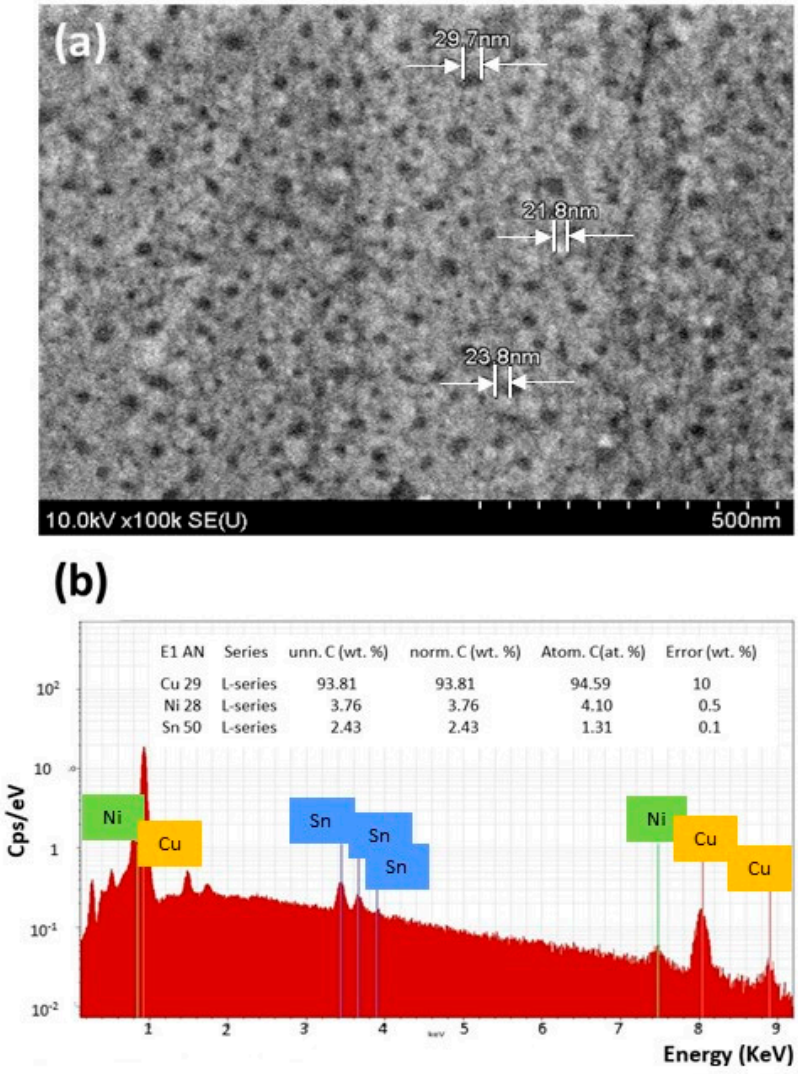

Figure 5. (**a**) SEM image of the electrode surface after Sn-Ni electrodeposition over 2 s at an applied potential of −0.32 V; (**b**) the corresponding EDX.

3.1. Influence of Current Density on Cathode Current Efficiency

In complex electrolytes, the variation in cathodic current yield is due to the process characteristics of the electrode surface. The evolution of the cathodic current yield as a function of the applied current density for a TiO_2NP-based alloy and composite coatings at a concentration of 1 g/L is shown in Figure 6.

It was found that as the current density increased from 0.5 to 4 A/dm^2, the cathodic current efficiency for the Sn-Ni alloy decreased from 99.8% to 53.9%. With the introduction of TiO_2NPs into the electrolyte composition, an approximately linear dependence of current efficiency on current density was observed. For a composite coating with TiO_2NPs, the current efficiency is much higher at high current densities, which may be due to an increase in electrolyte diffusion and a significant change in the composition of the coating phase. To confirm the latter hypothesis, the crystal phase and elemental composition of the Sn-Ni

alloy coatings at different current densities were investigated and the X-ray diffraction results are shown in Figure 7.

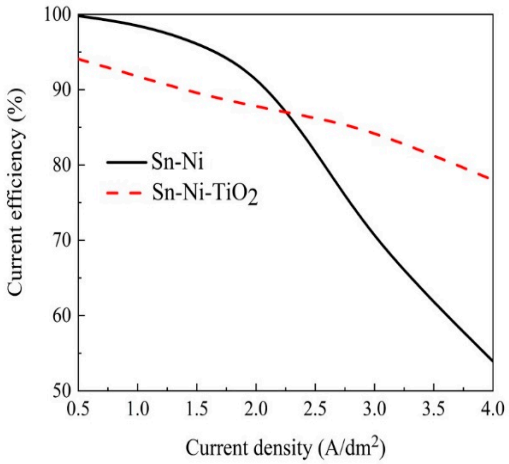

Figure 6. The current efficiency versus the current density for Sn-Ni and Sn-Ni-TiO_2 coatings.

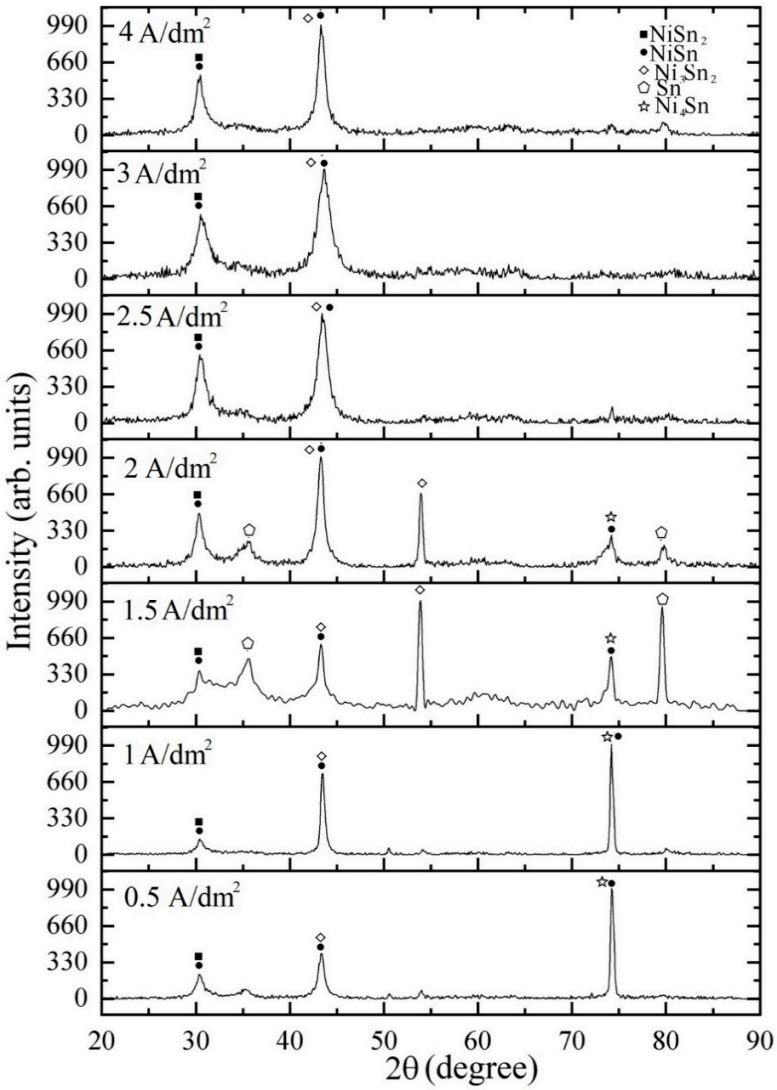

Figure 7. XRD patterns of coatings based on Sn-Ni alloy at different current densities.

Figure 7 shows that an increase in current density to 2.5 A/dm^2 is accompanied by a significant change in the phase composition of the coatings. It is also interesting to note that the Ni_4Sn intermetallic compound did not form at current densities above 2.5 A/dm^2, whereas a Sn peak was observed for coatings deposited at current densities of 1.5 A/dm^2 and 2 A/dm^2. It should be noted in Figure 8 that the Sn and Ni contents of the alloy also increase slightly with current. At current densities of 2 A/dm^2 and above, the Ni and Sn contents in the coating tend toward a 50/50 ratio.

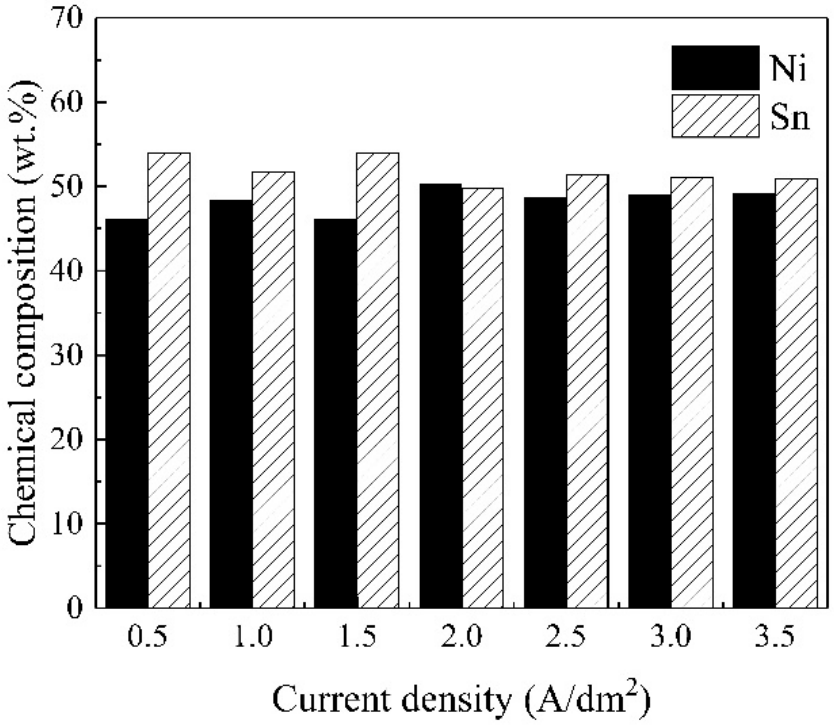

Figure 8. Elemental analysis of Sn-Ni coatings at different current densities.

Increasing the cathodic current density slightly affects the structure of the coatings and also leads to changes in the Sn/Ni ratio. The maximum Ni content in the alloy composition is observed at a current density of 2 A/dm^2 and amounts to 50.2 wt%, the minimum content is observed at a current density of 1.5 A/dm^2 and amounts to 46.06 wt%. These results show that an increase in cathodic current density induces Ni and Sn deposition in equivalent proportions. Another hypothesis to explain the behavior of chemical composition as a function of current density is the increase in the specific surface area of the electrode. Under the influence of the electric field resulting from the applied electrodeposition potential, TiO_2NPs covered with ionic adsorbates migrate toward the cathode surface where they are adsorbed. As a result, the positively charged particles adsorbed on the cathode surface increase the active surface area and provide more nucleation sites for Ni^{2+} ion reduction [50].

3.2. The Influence of TiO_2NP Concentration on the Structure and Composition of Deposited Coatings Based on Sn-Ni Alloy

The introduction of TiO_2NPs into the electrolyte also contributes to a change in the composition of the coating phase.

The XRD results in Figure 9 show the presence of Cu in the structure of the Sn coatings. This may be due to the diffusion of Sn into the Cu substrate structure and the formation of intermetallic compounds. TiO_2NP peaks are absent from the diffraction pattern, which can be explained by the relatively low concentration of TiO_2 in the composition of the electrolytes used to prepare the coatings. Figure 10 shows the diffractograms of the Sn-Ni alloy and the Sn-Ni-TiO_2NP alloy-based composite coating.

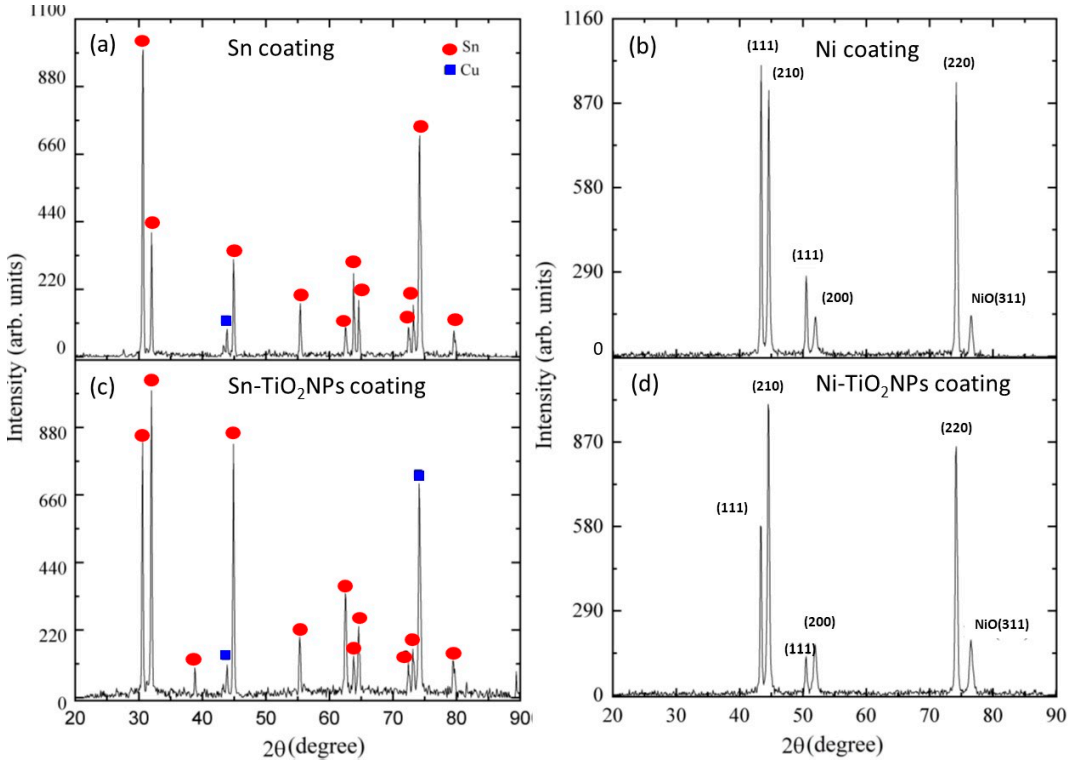

Figure 9. The diffractogram of different prepared coatings: (**a**) Sn, (**b**) Ni, (**c**) Sn-TiO_2NPs, and (**d**) Ni-TiO_2NPs.

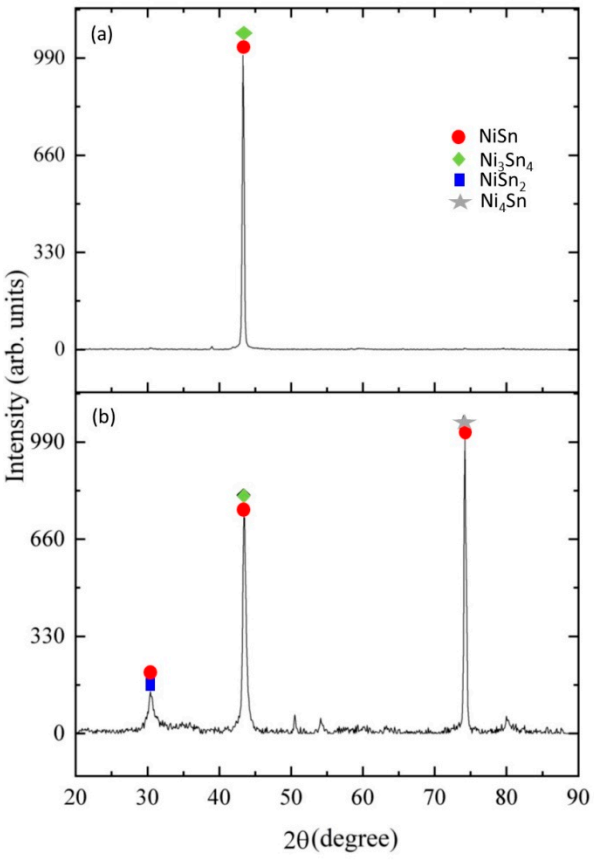

Figure 10. Diffractograms of (**a**) Sn-Ni and (**b**) Sn-Ni TiO_2NP coatings.

The XRD results in Figure 10 show that the Sn-Ni alloy is formed by several unstable intermetallic compounds such as NiSn, $NiSn_2$, Ni_3Sn_2, and Ni_4Sn. When TiO_2NPs are introduced into the electrolyte, the intensity of the main NiSn metastable peak changes. This can be explained by a slight change in the Sn content associated with a change in its solubility. The structure of the prepared coatings was also studied by SEM and the results are shown in Figure 11.

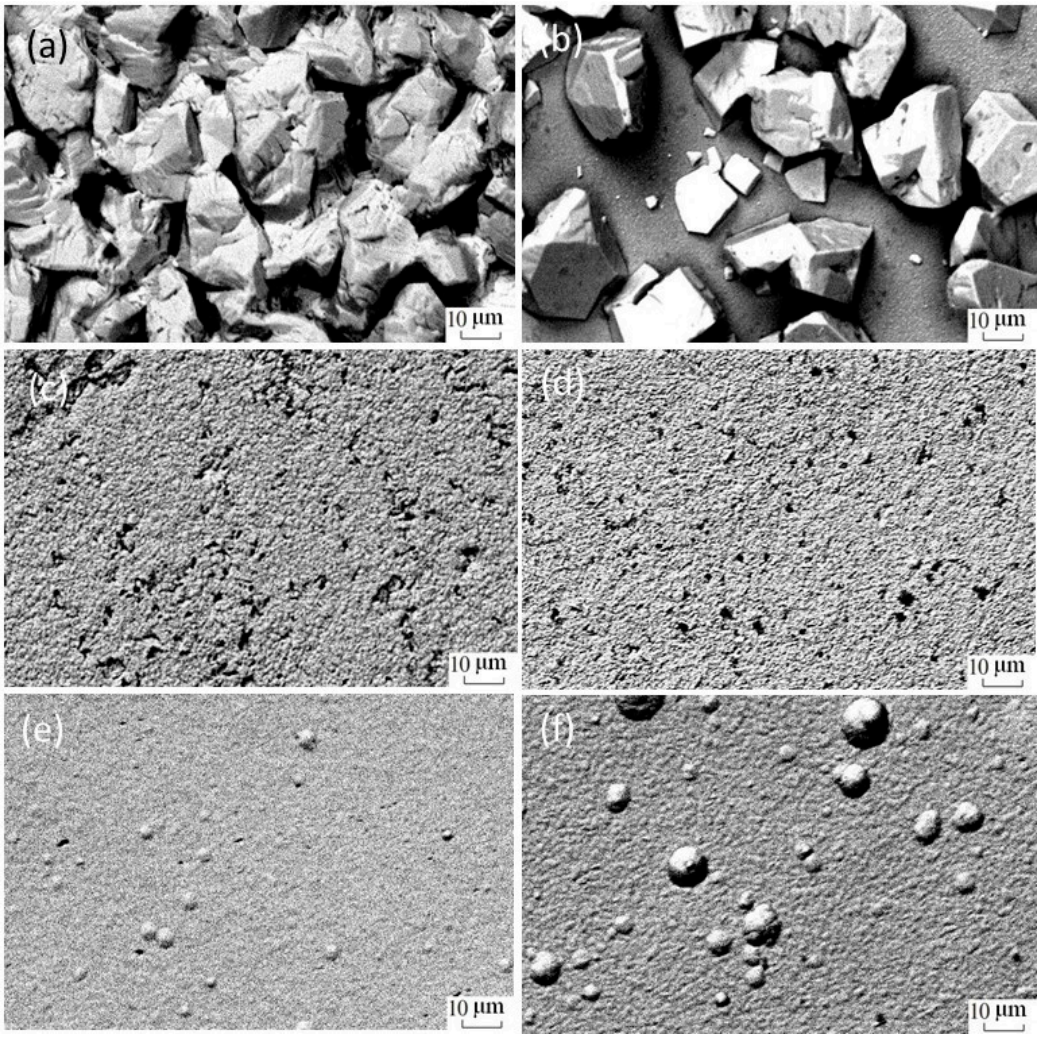

Figure 11. SEM images of different prepared coatings (**a**) Sn, (**b**) Sn-TiO_2NPs, (**c**) Ni, (**d**) Ni-TiO_2NPs, (**e**) Sn-Ni, and (**f**) Sn-Ni TiO_2NPs, at a current density of 1 A/dm^2.

The introduction of TiO_2NPs into the electrolyte leads to changes in the texture of the prepared coatings. It has been shown that in the case of Sn-TiO_2NPs deposition, more pronounced facet structures are observed compared to Sn deposition (Figure 11a,b). The Sn-TiO_2NP coating is inhomogeneous with the local formation of large Sn-TiO_2NPs about 20 µm larger than the Sn grains (Figure 11a) and larger than the size of the TiO_2NP aggregates (Figure 1). This may be due to hinderances of the Sn coating deposition when large TiO_2NP aggregates are deposited on the substrate surface as well as the rapid diffusion of Sn into the Cu substrate with the formation of new intermetallic compounds. In the case of Ni, when the TiO_2NPs are introduced into the electrolyte, the deposit has a uniform texture with fewer pores (Figure 11d). The Sn-Ni alloy coating is characterized by the formation of small spheroidal crystallites (Figure 11e). When TiO_2NPs are introduced into the electrolyte composition during the deposition of the Sn-Ni alloy, an increase in the size of the spheroids on the surface is observed, reaching diameters of the order of 10 µm

larger than the size of the TiO_2NPs aggregates (Figure 1a), which is the signature of local inclusion of TiO_2NPs in the coating (Figure 11f). The elemental and phase compositions of the prepared alloys and coatings are given in Table 3.

Table 3. Composition of different prepared coatings based on Sn, Ni, and Sn-Ni alloy with and without TiO_2NPs.

Coating	Element	Composition, wt.%
1	2	3
Sn	Sn	100
Sn TiO_2NPs	Sn Cu TiO_2	38.38 60.47 0.73
Ni	Ni	100
Ni TiO_2NPs	Ni TiO_2	99.87 0.13
Sn-Ni	Sn Ni	51.69 48.31
Sn-Ni TiO_2NPs	Sn Ni TiO_2	55.78 44.22 0

For single-metal coatings, deposited metal content reaches 100%. In the case of Sn-TiO_2NPs, the coating is characterized by an irregular structure and the intercrystallite contains Cu (Figure 11d). In addition, it has been shown that when TiO_2NPs at a concentration of 1 g/L are introduced into the Sn and Ni deposition electrolytes with ionic strength compensation, the TiO_2NPs are incorporated into the Sn and Ni coatings with a composition limit of 0.73 and 0.13 wt%, respectively. For the Sn-Ni alloy coating, the Sn and Ni contents are 51–56 wt% and 48 wt%, respectively. In the case of the composite alloy coating, TiO_2NPs are not detected in the coating composition. This may be due to their highly inhomogeneous inclusion in the coating composition in the form of agglomerates of TiO_2NP aggregates. As the EDX analysis did not reveal the presence of TiO_2NPs in the coating, an XRF analysis was carried out for confirmation (Table 4).

Table 4. Elemental content of indicated coatings.

Coating	Element	Composition, wt%
Sn-Ni	Ni Sn Cl	32.31 67.66 0.03
Sn-Ni TiO_2NPs (1 g/L)	Ni Sn Cl Ti	46.19 53.77 0.04 -
Sn-Ni-TiO_2NPs (2 g/L)	Ni Sn Cl Ti	37.26 62.59 0.03 0.12

Table 4 shows that Ti was not detected in the Sn-Ni TiO_2NP-based coating at a TiO_2NP concentration of 1 g/L in the electrolyte. However, by increasing the TiO_2NP concentration to 2 g/L in the electrolyte, the Ti content in the coating increases to 0.12 wt%, a signature that TiO_2NPs have been incorporated into a Sn-Ni TiO_2NP-based coating. To further investigate the presence of TiO_2NPs in the Sn-Ni TiO_2NP coating, Raman experiments were

carried out and the spectra are shown in Figure 12. Analysis of these spectra provided an estimate of the TiO_2NP content.

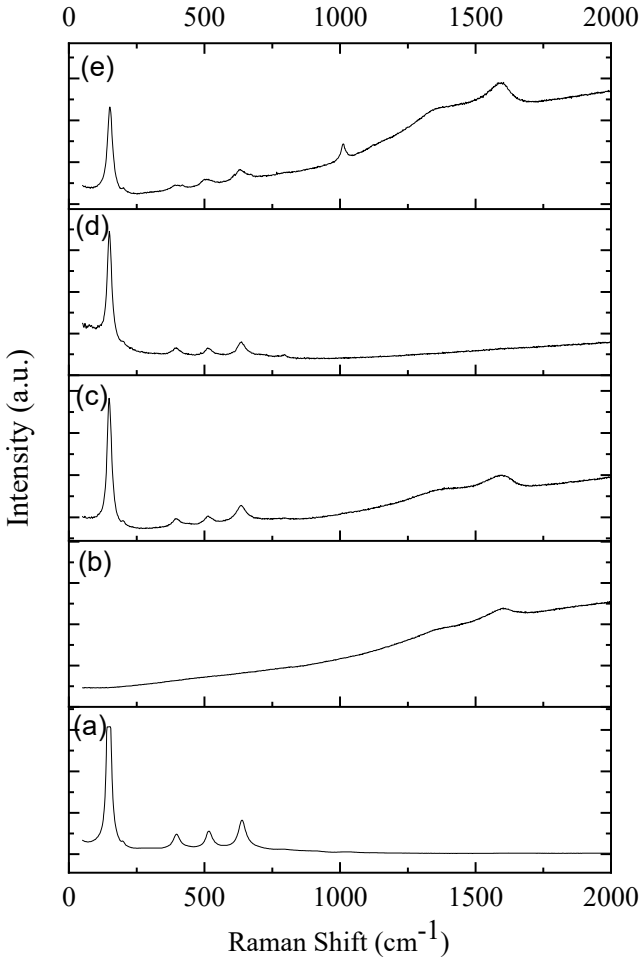

Figure 12. Raman spectra for (**a**) TiO_2NPs, (**b**) Sn-Ni, and composite coatings based on Sn-Ni alloy with different concertation of TiO_2NPs in the electrolyte (g/L): (**c**) 1, (**d**) 2, and (**e**) 5.

In the Raman spectra corresponding to Sn-Ni alloy-based composite coatings with the presence of TiO_2NPs in the deposition electrolyte, peaks were observed in the region of 150, 395, 512, and 634 cm^{-1} (Figure 12c,e), which are characteristic of TiO_2NPs (Figure 12a). This confirms the inclusion of TiO_2NPs in the composition of Sn-Ni alloy-based composite coatings and that the embedded TiO_2NPs increase with the concentration of TiO_2NPs in the electrolyte. In addition, these results show that Raman measurements are more sensitive to the presence of TiO_2NPs in Sn-Ni alloy-based composite coatings at concentrations lower than 1 g/L.

Furthermore, the introduction of TiO_2NPs into the composition of the deposition electrolyte for Sn, Ni, and Sn-Ni coatings was observed to have an ambiguous effect on the surface roughness of the prepatterned coatings (Figure S1).

With the introduction of TiO_2NPs into the deposition electrolyte composition, Sn and Ni coatings become rougher. However, for a Sn-Ni alloy-based composite coating, the microroughness decreases slightly. This can be explained by the uniform incorporation of TiO_2NPs into the alloy phase deposited over the entire surface as well as the absence of TiO_2NP agglomeration in the deposition electrolyte. Table 5 shows the surface microroughness for the different coatings studied.

Table 5. The main indicators of the microroughness of the surface of different prepared coatings.

Coating	R_a, μm	R_z, μm	R_{max}, μm
Sn	1.14	5.24	7.89
Sn-TiO_2NPs	3.54	13.11	20.73
Ni	0.21	1.04	1.37
Ni-TiO_2NPs	0.58	3.05	3.94
Sn-Ni	0.41	2.02	3.45
Sn-Ni-TiO_2NPs	0.34	1.66	2.97

It was found that by introducing 1 g/L of TiO_2NPs in the composition of the electrolyte for the deposition of Sn and Ni (with compensation of the ionic strength by a NaCl solution), the various parameters quantifying microroughness (R_a, R_{max}, and R_z) increased by almost three times. In the case of composite coatings based on Sn-Ni-TiO_2NPs alloys, the opposite effect was observed, i.e., a decrease in roughness. The dependence of the microroughness of Sn-Ni coatings on the deposition current density was also investigated and the results are shown in Figure 13.

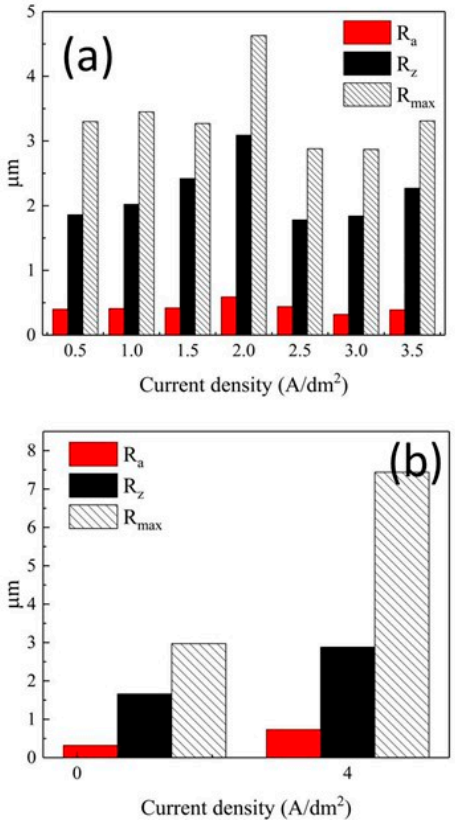

Figure 13. Microroughness of the surface of Sn-Ni coatings: (**a**) at different current densities, (**b**) Sn-Ni-TiO_2NPs coating (CEC) at current densities 1 and 4 A/dm^2.

The roughness results shown in Figure 13a indicate that maximum values of R_a, R_z, and R_{max} were obtained at a current density of 2 A/dm^2 while minimum values were observed at a current density of 3 A/dm^2. The irregular dependence of microroughness on current density may be related to a significant change in phase composition and degradation of coatings deposited at current densities above 3 A/dm^2. In the case of TiO_2NP-based composite coatings, the evolution of microroughness was studied at current densities of 1 and 4 A/dm^2, and the results are shown in Figure 13b. It can be observed that an increase in the current density of Sn-Ni-TiO_2NP coatings leads to an increase in the roughness parameters R_a, R_{max}, and R_z by a factor of 2 to 3. These results are in good

agreement with those obtained from the SEM characterization. The textures observed from the SEM characterization show an increase in the size of spheroids on the surface, which is a signature of the local inclusion of TiO_2NPs in the coating.

Surface roughness is a characteristic that has a major influence on the properties of the coating, particularly its optical and wetting properties. The physical interaction of a liquid with the surface of a solid or other liquid determines the wetting properties of that surface, and the degree of wetting is characterized by the wetting contact angle, θ, which is the angle formed by the plane tangent to the interfacial surfaces binding the wetting liquid, with the vertex of the angle lying on the line of separation of the three phases. Depending on this angle, a distinction is made between hydrophilic ($\theta < 90°$) and hydrophobic ($\theta > 90°$) surfaces. The value of the contact angle (θ), excluding the effect of gravity, depends solely on the molecular properties of the solid surface and the phases in contact with it. Figure 14 shows a diagram of the effect of current density on the wetting angles of Sn-Ni alloy coatings.

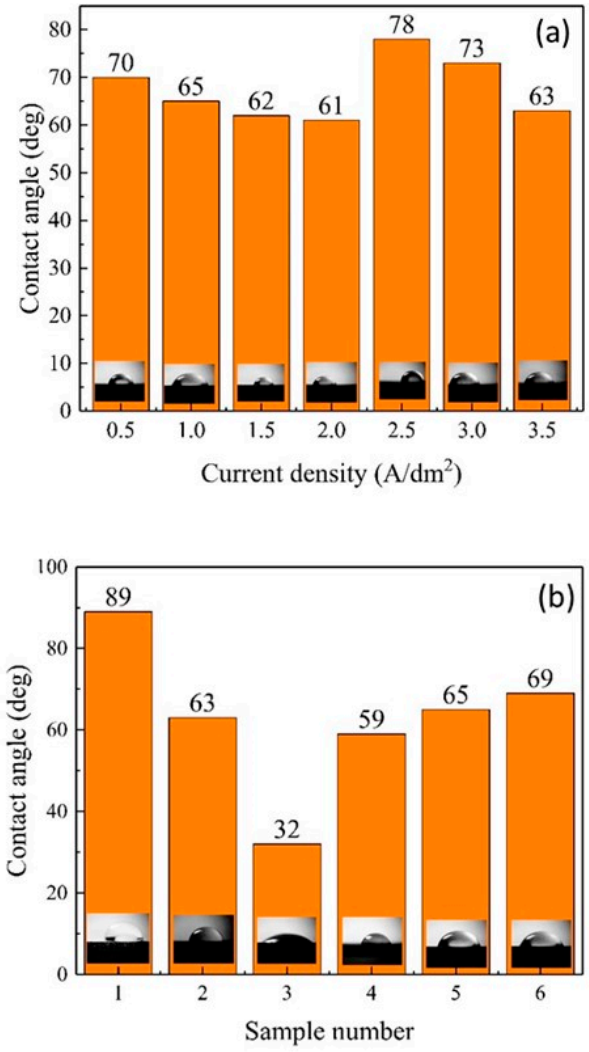

Figure 14. The contact angle of (**a**) the Sn-Ni coating at different current densities; (**b**) the studied coatings, 1—Sn, 2—Sn-TiO_2NPs, 3—Ni, 4—Ni-TiO_2NPs, 5—Sn-Ni, and 6—Sn-Ni-TiO_2NPs.

In Figure 14a, the results show that the variation in contact angle is inversely proportional to the variation in surface roughness. For coatings with the lowest roughness, obtained at a current density of 2.5 A/dm^2, the maximum value of the wetting angle was observed to be 78° ± 1.2. For Sn-Ni alloy-based coatings with higher roughness, obtained at a current density of 2 A/dm^2, the wetting contact angle reached minimum values of

around 61° ± 1.3°. Furthermore, the introduction of TiO_2NPs into the composition of the deposition electrolyte of Sn, Ni, and Sn-Ni-based coatings contributes to a modification of the wetting contact angle (Figure 14b).

As well as affecting surface roughness, the introduction of TiO_2NPs also contributes to changes in the composition and structure of the coatings. TiO_2NPs introduced into the electrolyte composition for the deposition of Sn-based coatings result in a 1.4-fold decrease in contact angle. For Ni and Sn-Ni alloy coatings, the introduction of TiO_2NPs into the electrolyte composition increases the contact angle by 2 and 1.1 times, respectively. The dependence of the Sn-Ni alloy wetting contact angle on the microroughness of the coatings studied was determined. The optimum current density of 1/dm^2 was used to obtain a wetting contact angle of about 65 ± 1.2°. The dependence of the TiO_2NPs incorporation on the contact angles of the prepared coatings was evaluated. It was found that the introduction of 1 g/L TiO_2NPs into the composition of the Sn-Ni alloy deposition electrolyte imparts hydrophobic properties to the surface.

3.3. Corrosion Properties

Since these coatings can modify objects in massive contact with human skin, evaluation of their corrosion resistance in artificial sweat was carried out using electrochemical impedance spectroscopy. The impedance spectra in an artificial sweat medium (pH = 7) are shown in Figure 15.

From the Nyquist and Bode diagrams in Figure 15, it is clear that in the absence of TiO_2NPs in the composition of Sn coatings, higher resistance values are observed. The charge transfer resistance (low-frequency region) of Sn coatings is 1.40 × 10^4 Ω·cm^2, however, with the introduction of TiO_2NPs, the resistance decreases to 7.90 × 10^3 Ω·cm^2 (Table 5). An opposite behavior was observed with the introduction of TiO_2NPs into the electrolyte composition for Ni deposition; an increase in the charge transfer resistance of the coating from 8.3 × 10^3 to 2.10 × 10^4 Ω·cm^2 was observed. In the case of Sn-Ni alloy-based coatings, with the introduction of TiO_2NPs, charge transfer resistance decreases from 4.25 × 10^4 to 3.7 × 10^4 Ω·cm^2. The impedance spectra were analyzed using the equivalent circuit shown in the insert of Figure 15a. The parameters obtained from the simulation of the impedance spectra using the equivalent circuit are shown in Table 6.

Introducing TiO_2NPs into the electrolytes when depositing Sn and Sn-Ni coatings reduces the charge transfer resistance at the interface, whereas, for Ni coatings, the introduction of 1 g/L of TiO_2NPs into the electrolyte composition doubles the charge transfer resistance. For all the coatings studied, the introduction of TiO_2NPs into the deposition electrolyte composition results in a slight decrease in the exponent n1 of the CPE1 element, with values between 0.7 and 0.91, indicating the capacitive nature of the element.

To further assess the anticorrosion properties of the prepared coatings, the potentiodynamic polarization technique was used, and the results are shown in Figure 16. The results were analyzed using the Tafel equation to determine the corrosion current and potential (Table 7).

Table 6. Parameters of the equivalent circuits of the impedance spectra for coatings Sn, Ni, Ni–Sn, Sn-TiO_2NPs, Ni-TiO_2NPs, and Sn-Ni TiO_2NPs obtained in an artificial sweat medium.

Coating	R_s (Ω cm^2)	R_1 (Ω cm^2)	Y_1 (Ω^{-2} cm^{-2}s^n)	n_1	R_2 (Ω cm^2)	Y_2 (Ω^{-2} cm^{-2}s^n)	n_2
Sn	18.74	11,300	1.53 × 10^{-5}	0.8	3000	5.93 × 10^{-4}	0.5
Sn-TiO_2NPs	5.03	7450	5.03 × 10^{-5}	0.78	1000	4.43 × 10^{-4}	0.15
Ni	12.53	6277	1.9 × 10^{-4}	0.8	832.9	1.77 × 10^{-5}	0.79
Ni-TiO_2NPs	13.57	19,277	7.93 × 10^{-5}	0.7	3833	5.16 × 10^{-5}	0.89
Sn-Ni	11.5	33,053	4.98 × 10^{-5}	0.91	9896	7.96 × 10^{-5}	0.62
Sn-Ni-TiO_2NPs	18.04	25,067	3.65 × 10^{-5}	0.79	8891	5.13 × 10^{-5}	0.51

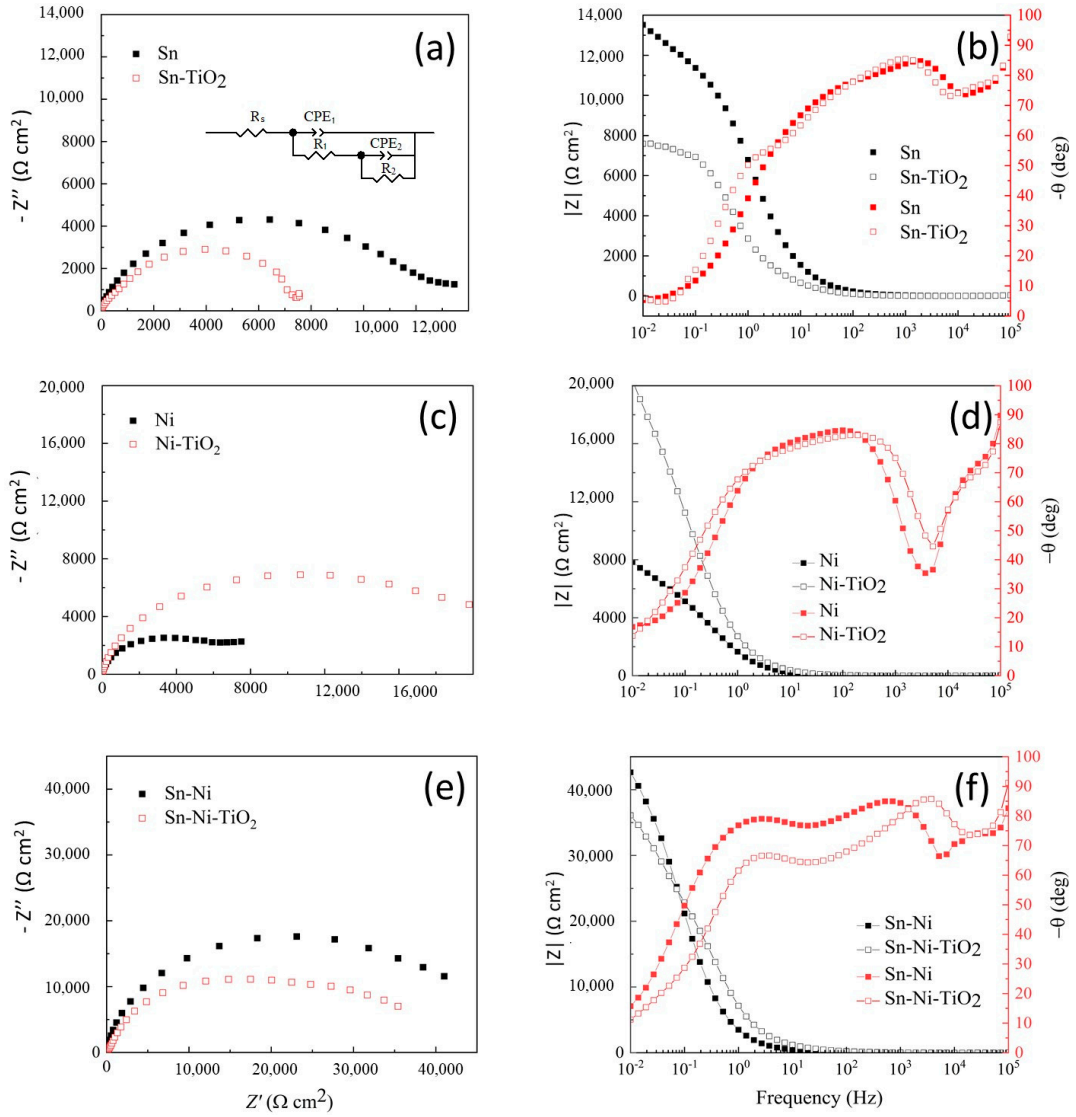

Figure 15. Nyquist and Bode diagrams of different prepared coatings as indicated in an artificial sweat medium: (**a**) Sn and Sn-TiO_2NPs (Nyquist), (**b**) Sn and Sn-TiO_2NPs (Bod), (**c**) Ni and Ni-TiO_2NPs (Nyquist), (**d**) Ni and Ni-TiO_2NPs (Bod), (**e**) Sn-Ni and Sn-Ni-TiO_2NPs (Nyquist), and (**f**) Sn-Ni and Sn-Ni-TiO_2NPs (Bode). The (**a**) insert corresponds to the equivalent circuit of an electrochemical cell for modeling impedance spectra. R_s—solution resistance, CPE_1—capacitive-type constant phase element, R_1—charge transfer resistance at the interface, CPE_2—diffusion-type constant phase element, R_2—diffusion resistance.

Table 7. Electrochemical parameters of corrosion of the studied samples.

Coating	I_{corr} (A/cm^2)	E_{corr} (V)	a_a (V)	b_a (V)	$\lvert a_c \rvert$ (V)	$\lvert b_c \rvert$ (V)
Sn	1.36×10^{-4}	−0.42	0.20	0.06	0.64	0.06
Sn-TiO_2NPs	1.17×10^{-4}	−0.35	0.21	0.04	0.46	0.03
Ni	4.84×10^{-5}	0.13	0.23	0.02	0.03	0.04
Ni-TiO_2NPs	4.87×10^{-5}	0.17	0.39	0.05	0.10	0.06
Sn-Ni	1.82×10^{-4}	0.08	0.36	0.08	0.16	0.06
Sn-Ni-TiO_2NPs	2.63×10^{-5}	−0.2	0.06	0.03	0.67	0.10

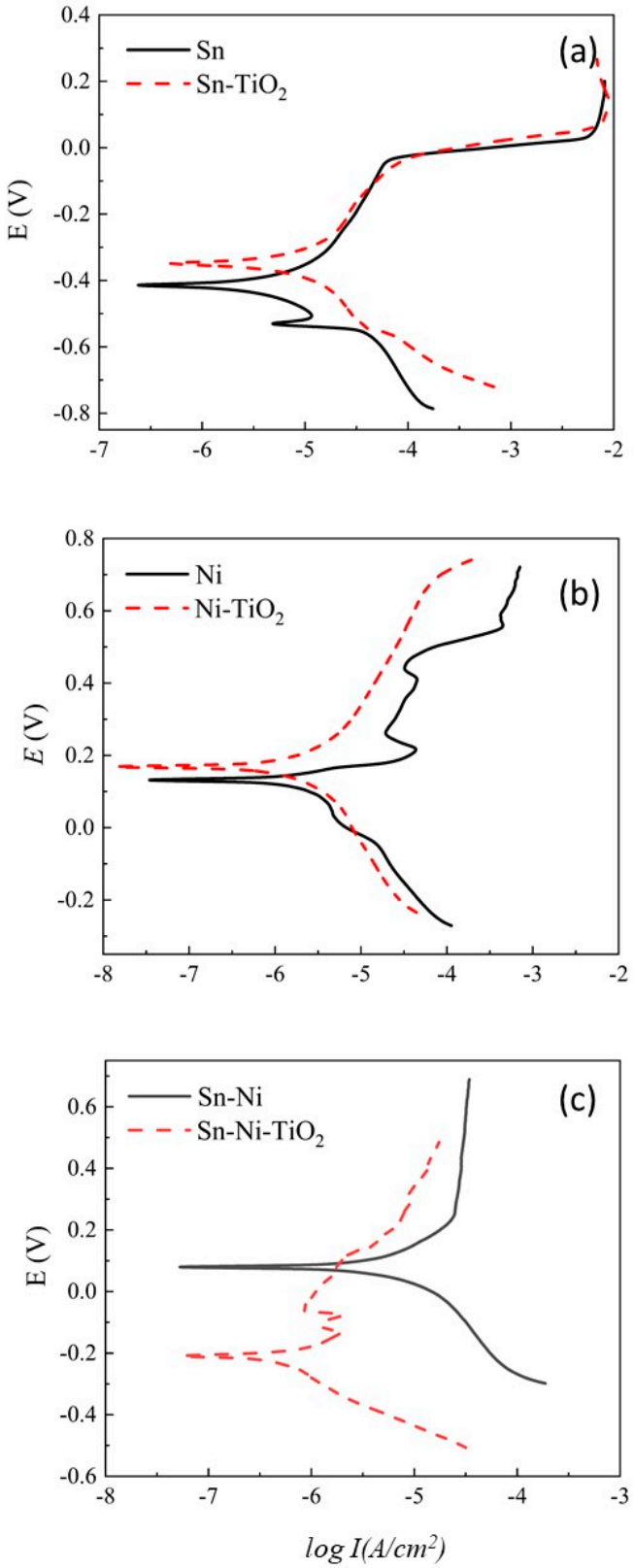

Figure 16. Potentiodynamic polarization curves of the corrosion process in an artificial sweat media of different prepared coatings as indicated (**a**) Sn and Sn-TiO_2, (**b**) Ni and Ni-TiO_2, and (**c**) Sn-Ni and Sn-Ni-TiO_2.

The introduction of TiO_2NPs into the deposition electrolyte of the Sn-based coating induces a shift in corrosion potential (E_{corr}) by 70 mV towards the electropositive region,

from E_{corr} (Sn) = −0.42 V to E_{corr} (Sn-TiO_2NPs) = −0.35 V, whereas this shift is only about 40 mV in the case of a Ni coating. The E_{corr} increased from 0.14 V for the Ni coating to 0.18 V for the Ni-TiO_2NP coating. In the latter case, corrosion current densities (I_{corr}) are 4.84×10^{-6} A/cm^2 and 4.87×10^{-5} A/cm^2, respectively. Figure 16c shows that in the case of the Sn-Ni alloy coating, the introduction of TiO_2NPs into the electrolyte during deposition of the Sn-Ni alloy coating induces a shift in the E_{corr} by 300 mV towards the electronegative region, from 0.09 V (Sn-Ni) to −0.21 V (Sn-Ni-TiO_2NPs); the corresponding I_{corr} are 1.82×10^{-4} A/cm^2 and 2.63×10^{-5} A/cm^2, respectively. The results of the main corrosion process parameters in an artificial sweat environment with a pH of 7 are presented in Table 7.

The E_{corr} of Sn- or Ni-based coatings changes insignificantly with the introduction of TiO_2NPs into the electrolyte composition, while in the case of Sn-Ni-based coatings, the corrosion current decreases 6.9-fold. The results of electrochemical impedance spectroscopy of the coatings in a 3% NaCl solution are shown in Figure 17. It can be seen that the Nyquist diagrams obtained for all the coatings studied in the NaCl medium are characterized by a capacitive semicircle in the high- and mid-frequency regions.

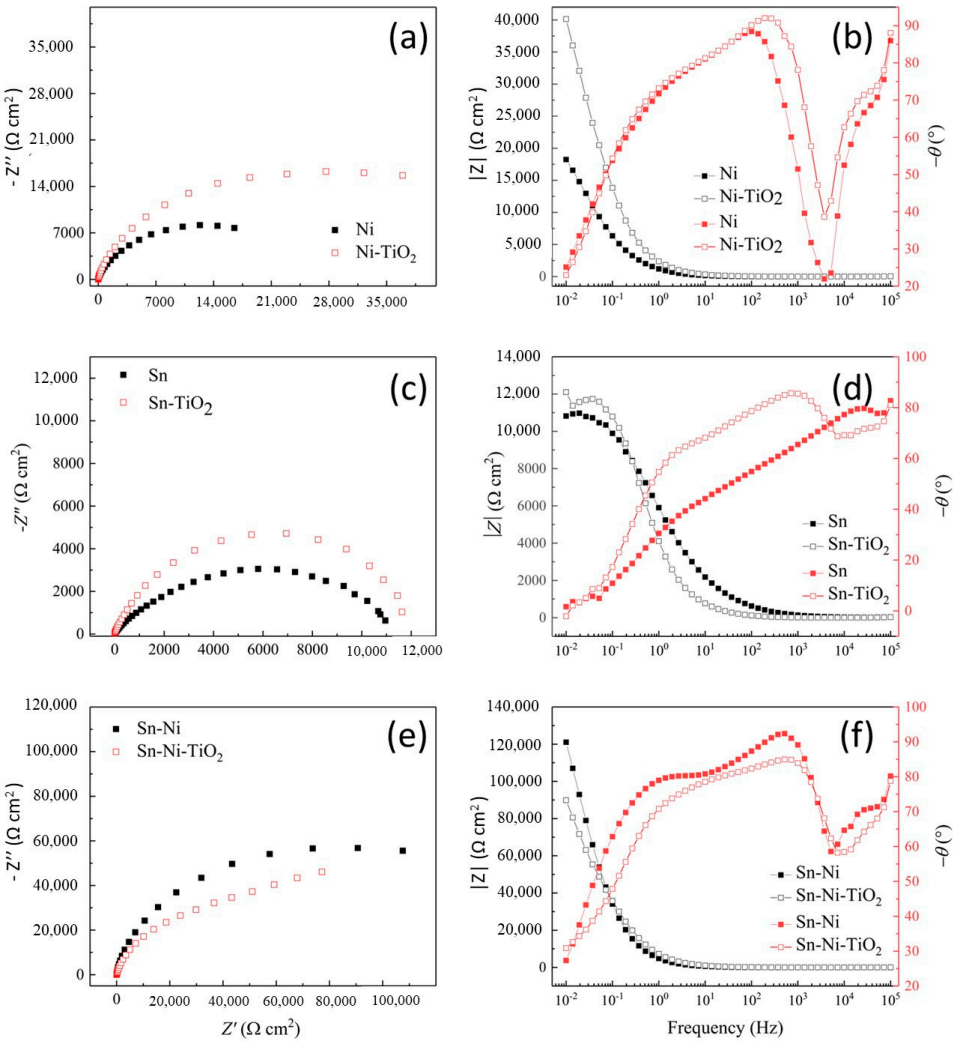

Figure 17. Nyquist diagrams of different prepared coatings in 3% NaCl solution as indicated (**a**) Ni and Ni-TiO_2NPs, (**c**) Sn and Sn-TiO_2NPs, and (**e**) Sn-Ni alloy, and Sn-Ni-TiO_2NPs). The corresponding Bode diagrams in the same solution are indicated as follow: (**b**) Ni and Ni-TiO_2NPs, (**d**) Sn and Sn-TiO_2NPs, and (**f**) Sn-Ni alloy, and Sn-Ni-TiO_2NPs.

In the case of Ni-based coatings, it can be seen in Figure 17a,b that the introduction of TiO_2NPs into the deposition electrolyte induces a higher increase in charge transfer resistance from 1.80×10^4 to 4.0×10^4 Ω·cm^2, whereas, the Bode diagrams (Figure 17d) show a slight increase in charge transfer resistance from 1.10×10^4 to 1.20×10^4 Ω·cm^2, in the case of Sn-based coatings with embedded TiO_2NPs (low-frequency region). For Sn-Ni alloy-based coatings (Figure 17e,f), the introduction of TiO_2NPs into the deposition electrolyte induces the charge transfer resistance, which decreases from 1.20×10^5 to 9.0×10^4 Ω cm^2. The parameters obtained from the equivalent circuit analysis of the impedance spectra are shown in Table 8.

Table 8. Parameters of equivalent circuits used to analyze the impedance spectra of different prepared coatings (Sn, Ni, Sn-Ni, Sn-TiO_2NPs, Ni-TiO_2NPs, and Sn-Ni-TiO_2NPs) in solution 3% NaCl.

Coating	R_s, (Ω cm^2)	R_1, (Ω cm^2)	Y_1, (Ω^{-2} cm^{-2}s^n)	n_1	R_2, (Ω cm^2)	Y_2, Ω^{-2} (cm^{-2}s^n)	n_2
Sn	7.89	10,188	3.6×10^{-5}	0.61	1465	1.7×10^{-6}	0.77
Sn-TiO_2NPs	11.89	11,324	3.3×10^{-5}	0.82	1024	5.15×10^{-5}	0.86
Ni	11.62	21,679	1.95×10^{-4}	0.76	1918	1.24×10^{-5}	0.33
Ni-TiO_2NPs	13.42	44,679	6.95×10^{-5}	0.74	4118	1.42×10^{-5}	0.43
Sn-Ni	11.98	145,600	3.91×10^{-5}	0.8	18,286	5.57×10^{-5}	0.64
Sn-Ni-TiO_2NPs	12.58	75,240	3.7×10^{-5}	0.82	30,001	8.99×10^{-5}	0.78

The introduction of TiO_2NPs into the electrolytes for the deposition of Ni and Sn coatings increases the resistance to charge transfer at the interface. For a Sn-NiTiO_2NP composite coating with 1 g/L TiO_2NPs in the electrolyte composition, the charge transfer resistance indicators decrease by a factor of two. For Ni coatings, the introduction of TiO_2NPs into the composition of the deposition electrolyte decreases the exponent n of the CPE_1 element slightly but for Sn-TiO_2NPs and Sn-Ni-TiO_2NPs this exponent increases. The n_1 index is in the range of 0.61 to 0.82, which indicates the presence of defects in the coating.

The results of potentiodynamic polarization curves are presented in Figure 18 for the different prepared coatings. Based on these results, the corrosion currents and the corrosion initiation potential were calculated.

Analysis of the potentiodynamic polarization curves showed that the corrosion potential of the Sn-based coating (Figure 18a) is −0.22 V and that the introduction of TiO_2NPs into the deposition electrolyte composition resulted in a 110 mV shift in potential towards the electronegative region, reaching a value of −0.33 V. It can also be observed that the corrosion current density is 1.03×10^{-4} A/cm^2 and 6.48×10^{-5} A/cm^2 for Sn and Sn-TiO_2NPs coatings, respectively. In the case of Ni coatings, it was observed that the corrosion potential is 0.05 V, but when TiO_2NPs are introduced into the deposition electrolyte, the corrosion initiation potential shifts by 230 mV towards the electronegative region and reaches a value of −0.18 V. The corrosion current densities corresponding to the Ni- and Ni-TiO_2NP-based coatings are 2.39×10^{-5} A/cm^2 and 2.18×10^{-5} A/cm^2, respectively (Figure 18b). Figure 18c shows that TiO_2NPs introduced into the Sn-Ni alloy deposition electrolyte shift the corrosion initiation potential by 100 mV toward the electropositive potentials, from 0.08 V to −0.02 V. Furthermore, the corrosion currents are 1.01×10^{-4} A/cm^2 and 9.94×10^{-6} A/cm^2 for Sn-Ni and Sn-Ni-TiO_2NPs, respectively. The main parameters characterizing the corrosion process are shown in Table 9.

The introduction of TiO_2NPs into the deposition electrolyte compositions of all coatings was accompanied by a more or less pronounced decrease in corrosion current. The corrosion currents of Sn-Ni alloy and Ni-based coatings do not change significantly with TiO_2NPs in the deposition electrolyte composition. In the case of Sn coatings, the corrosion current density decreases by a factor of 1.6.

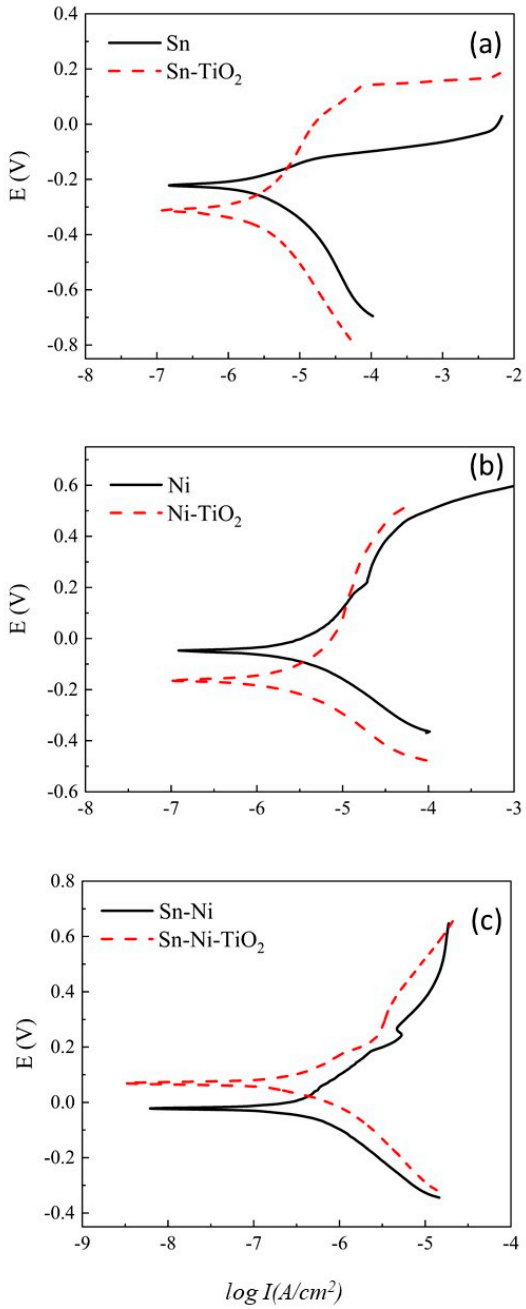

Figure 18. Potentiodynamic polarization curves of the corrosion process in a solution of 3% NaCl for prepared coatings as indicated: (**a**) Sn and Sn-TiO_2 coatings, (**b**) Ni and Ni-TiO_2 coatings, and (**c**) Sn-Ni and Sn-Ni-TiO_2 coatings.

According to these results, obtained both in an artificial sweat medium and a 3% NaCl solution, the different coatings prepared show different trends in terms of anticorrosion properties when TiO_2NPs are added to the deposition electrolyte. Indeed, TiO_2NPs incorporated in Sn, Ni, and Sn-Ni coatings modify their anticorrosion properties, which can be explained by their surface-wetting properties and their chemical composition. As shown by SEM surface characterization, the surface texture changes with the introduction of TiO_2NPs, which consequently influences their roughness and wetting properties. It is well known in the literature that a surface with an increased contact angle reduces the area of contact with the liquid on its surface, which can lead to a reduction in the surface area in contact with the aggressive medium and therefore its corrosion [52,53]. Bearing this in mind, the results obtained can be explained as follows.

Table 9. Electrochemical Tafel parameters of the studied coatings in a solution of 3% NaCl.

Coating	I_{corr}, A/cm^2	E_{corr}, V	a_a, B	b_a, B	$\lvert a_k \rvert$, B	$\lvert b_k \rvert$, B
Sn	1.03×10^{-4}	−0.22	0.048	0.066	0.606	0.098
Sn-TiO_2	6.48×10^{-5}	−0.33	0.145	0.112	0.601	0.066
Ni	2.39×10^{-5}	0.05	0.483	0.095	0.792	0.181
Ni-TiO_2	2.18×10^{-5}	−0.18	0.025	0.032	0.378	0.044
Sn-Ni	1.01×10^{-5}	−0.02	0.18	0.04	0.298	0.056
Sn-Ni-TiO_2	9.95×10^{-6}	0.08	0.33	0.051	0.329	0.081

In the case of the Sn coating, the decrease in corrosion resistance can be explained by the decrease in the contact angle and, therefore, an increase in the surface area exposed to corrosion processes. Furthermore, the increase in corrosion resistance of the Ni-based coating after the incorporation of TiO_2NPs is due to the synergistic effect between the increase in contact angle—and therefore minimization of the contact surface with the aggressive solution—and the anticorrosive property of the chemical element Ni. In the case of the Sn-Ni-based coating, it was observed that the corrosion resistance decreased after the introduction of TiO_2NPs, despite a relatively high contact angle compared to the other coatings and the presence of the chemical element Ni. This can be explained by the appearance of porosity in the coating after the incorporation of TiO_2NPs, which can facilitate the penetration of the aggressive solution through the coating, reaching a maximum surface area susceptible to being corroded.

Antibacterial properties are strongly recommended for surfaces in public areas that come into contact with human skin. TiO_2NPs are materials with high photocatalytic properties and, when used in coatings, impart antibacterial properties. The antibacterial properties of the coatings prepared in this work have been investigated and are presented in Table 10.

Table 10. The antibacterial activity of samples, evaluated using the St. aureus ATCC 6538 test.

Sample	Concentration of Bacterial Cells C (CFU/mL)		Reduction Factors (RF)
	Under UV Irradiation	Without UV Irradiation	
Sn-Ni (control)	3.3×10^3	1.4×10^6	2.6
Sn-Ni-TiO_2NPs	2.0×10^1	5.0×10^5	4.4
Ni	7.0×10^1	1.3×10^6	4.3
Ni-TiO_2NPs	4.0×10^1	9.9×10^5	4.4
Sn	3.0×10^1	4.4×10^5	4.1
Sn-TiO_2NPs	2.0×10^1	1.1×10^6	4.7
Sn-Ni-TiO_2NPs (Degussa)	8.0×10^1	1.6×10^5	3.3

According to the antibacterial test presented in Table 10, the prepared coatings show bactericidal activity with an RF parameter > 2; in addition, the coatings show that under UV light they can reduce the concentration of microorganisms by 4 to 5 orders of magnitude. Furthermore, the antibacterial activity of Sn-based coatings is due to the presence of copper with antibacterial properties in the coating composition as Sn has no antibacterial properties. Figure S2 shows the antibacterial properties of the coatings studied with the St. aureus disease bacterium test.

Experiments have shown that for all coatings, the introduction of TiO_2NPs into the composition of the deposition electrolytes, and consequently into the coatings, leads to an enhancement of the antibacterial properties with and without UV radiation.

Table 11 shows that the introduction of TiO_2NPs (1 g/L) into the deposition electrolyte for the deposition of Sn, Ni, and Sn-Ni coatings leads to an increase in the antibacterial properties under UV radiation in the presence of *E. coli* ATTC 8739 strains but with a lower efficiency than those observed using the St. John's strains. Electrochemical composite

coatings with TiO_2NPs were shown to have the best biocidal properties against Gram-positive and Gram-negative strains. They can be widely used on objects that are accessible to humans in public environments.

Table 11. The antibacterial activity of samples, evaluated using *E. coli* ATTC 8739 tests.

Sample	Concentration of Bacterial Cells C, CFU/mL		Reduction Factors (RF)
	Under UV Irradiation	Without UV Irradiation	
Sn-Ni (control)	5.4×10^3	3.9×10^5	1.9
Sn-Ni-TiO_2	3.4×10^2	9.0×10^4	3.4
Ni	3.6×10^2	1.5×10^5	2.6
Ni-TiO_2	6.0×10^1	2.5×10^5	3.6
Sn	1.9×10^2	4.6×10^4	2.3
Sn-TiO_2	1.6×10^3	5.9×10^5	2.6
Sn-Ni-TiO_2 (Degussa)	8.0×10^1	2.5×10^5	3.4

To assess the antibacterial properties of a solid surface, several factors must be taken into account, such as the properties of the surface in terms of hydrophobicity, roughness, and chemical composition as well as the bacterial species. The proliferation of bacteria on a solid surface is affected by the configuration and roughness of the surface, which has a strong influence on the adhesion of bacteria to the solid surface and their viability. Bacterial attachment to solid surfaces is considered to be the first step in bacterial growth and proliferation. It has been widely demonstrated that poor bacterial adhesion to a solid surface leads to bacterial death. Therefore, weakening bacterial adhesion is considered one of the indirect approaches to prevent bacterial proliferation. Surface patterning and roughness can increase the hydrophobic character of the surface, causing bacteria to repel and weakly adhere to the solid surface, leading to their death.

A further method of preventing bacterial proliferation, which is regarded as a direct approach, is to regulate the chemical composition of the surface. The metallic surface of nanoparticles (NPs) such as Zn, Al, Ni, Zr, Ce, Mg, and TiO_2 have antibacterial properties [54–59]. In particular, the photoelectrochemical and photocatalytic properties of TiO_2 nanoparticles [59,60] have been shown to enable them to generate electron-hole pairs that can react with water or oxygen to produce reactive oxygen species (ROS) such as superoxide anions, hydrogen peroxide, and hydroxyl radicals. The latter species can penetrate bacterial cell walls and cause cell death by disrupting cell function [61–67]. Several studies in the literature have reported that TiO_2NPs have strong antibacterial and antifungal activity against many Gram-positive bacteria such as Staphylococcus aureus and Gram-negative bacteria such as Escherichia coli [68,69].

In addition, Ni nanocrystals have been reported to have antibacterial activity against Gram-positive/negative bacteria and bacterial spores such as *Staphylococcus aureus* (*S. aureus*) and *Escherichia coli* (*E. coli*). Although the mechanism of the antibacterial effect of Ni nanocrystals is not yet fully understood, it has been reported that during the interaction between the Ni surface and bacteria, Ni^{2+} leaching has been detected, which penetrates the bacterial membrane and generates reactive oxygen species, leading to disruption of its function and bacterial death [70]. In the case of the Sn surface, it has been reported to exhibit weak antibacterial activity when exposed to *Staphylococcus aureus* (*S. aureus*) or *Escherichia coli* (*E. coli*) bacteria [71].

To understand the antibacterial test results of the coating prepared with and without TiO_2NPs, it is necessary to consider the synergistic effect of the two factors influencing the antibacterial activity of the solid surface mentioned above. There is a synergistic effect between the weakening of the bacteria adhesion due to the hydrophobicity of the surface on the one hand and the antibacterial properties of the chemical elements of the solid surface on the other. In the case of Sn with low antibacterial activity, the observed result could be explained by the hydrophobicity of the surface leading to weak adhesion of the bacteria

and their death at a later stage. The incorporation of TiO_2NPs into the Sn coating results in a decrease in contact angle from 89° to 63° and an increase in bacterial adhesion to the surface; however, the antibacterial activity of the TiO_2NPs effectively compensates for this effect, thereby explaining the relatively minor change in FR from 2.3 to 2.6.

For Ni and Sn-Ni coatings, the strong increase in FR after incorporation of TiO_2NPs could be explained by the synergistic effect of the antibacterial properties of Ni and TiO_2NPs rather than by the low adhesion of bacteria to the surface. The Ni coating exhibits hydrophilic properties (a contact angle of 32°), which facilitate bacterial adhesion. However, the extensive contact area between the bacteria and the Ni hydrophilic surface ensures the coating's antibacterial efficacy. Furthermore, the integration of TiO_2 NPs into the Sn-Ni coating leads to a negligible alteration in the contact angle (Figure 15), suggesting that the bacterial adhesion strength remains comparable. The observed antibacterial activity is primarily attributed to the synergistic effect of Ni and TiO_2 NPs.

The results demonstrate that Sn, Ni, and TiO_2NPs are crucial for the development of coatings with enhanced anticorrosion and antibacterial properties. The Sn-Ni-TiO_2 coating exhibits an effective antibacterial activity (RF 3.4) and anticorrosion performance, characterized by a more positive Ecorr (0.08 V), a lower current density (9.95×10^{-6} A/cm^2), and a higher charge transfer resistance (25,067 $\Omega \cdot$cm^2).

A comparative analysis of our Ni-Sn-based coatings, prepared with the incorporation of low concentrations of TiO_2 NP aggregates (1 g/L)—with similar coatings identified in the existing literature [35,36]—has revealed that the performance of the current coatings is highly promising, exhibiting significant resistance to corrosion in an artificial sweating environment and to bacterial proliferation.

4. Conclusions

It has been demonstrated that the mechanism by which deposited coatings form is consistent with the electrochemical behavior of instantaneous growth, and the three-dimensional growth is controlled by ion diffusion. Furthermore, it was observed that the introduction of TiO_2NPs did not affect the potentiodynamic polarization curves but significantly modified the phase composition and structure of the coatings formed. Additionally, the deposition current density of the alloy was found to influence the coating yield, elemental and phase composition, and wetting properties of the coatings studied.

In coatings deposited at a current density of 0.5 to 1.5 A/dm^2, Sn is the predominant element in the coating composition, representing up to 55% by weight. The anticorrosion properties of Sn-Ni alloy-based coatings were investigated in an artificial sweat medium. The incorporation of TiO_2NPs at a concentration of 1 g/L into the deposition electrolyte resulted in a notable reduction in the initial current density, which demonstrates the efficacy of these nanoparticles in their contribution to corrosion inhibition.

The introduction of TiO_2NPs into the composition of deposition electrolytes has been demonstrated to enhance the biocidal properties of the resulting coatings, both with and without UV radiation. This makes them suitable for use on objects in public settings that frequently come into contact with people.

The combined effect of chemical composition and surface roughness has been demonstrated to enhance the anticorrosive and bactericidal properties of the prepared coatings.

Supplementary Materials: The following supporting information can be downloaded at: https://www.mdpi.com/article/10.3390/coatings14111344/s1, Figure S1. Microroughness of (a) Sn, (b) Ni, and (c) Sn-Ni coatings with and without TiO_2NPs as indicated. Figure S2. Antibacterial properties in terms of the bacteria St. aureus test of different prepared coatings with and without UV exposition as indicated.

Author Contributions: Conceptualization, A.C. and A.T.; Methodology H.P.; Validation, A.T. and Y.X.; Investigation, M.V., H.P., and O.A.; Data curation, O.A.; Writing—original draft, H.P. and V.P.B.; Formal analysis, M.V., H.P. and V.P.B.; Writing—review and editing, A.T. and Y.X.; Supervision, A.C. and A.T. All authors have read and agreed to the published version of the manuscript.

Funding: This research was funded by grant of the Ministry of Education of the Republic of Belarus, grant number 24-038 «Electrochemical production and physical–chemical properties of nickel–cobalt alloy».

Institutional Review Board Statement: Not applicable.

Informed Consent Statement: Not applicable.

Data Availability Statement: The data presented in this study are available on request from the corresponding author.

Acknowledgments: The authors acknowledge the Ministry of Education of the Republic of Belarus for supporting the achievement of this work.

Conflicts of Interest: The authors declare no conflict of interest.

References

1. Pop, A.B.; Iepure, G.; Titu, A.M.; Ravai-Nagy, S. Characterization and corrosion behavior of zinc coatings for two anti-corrosive protections: A detailed study. *Coatings* **2023**, *13*, 1460. [CrossRef]
2. Klapper, H.S.; Zadorozne, N.S.; Rebak, R.B. Localized corrosion characteristics of nickel alloys: A review. *Acta Metall. Sin. (Engl. Lett.)* **2017**, *30*, 296–305. [CrossRef]
3. Shi, T.; Liang, J.; Li, X.; Zhang, C.; Yang, H. Improving the corrosion resistance of aluminum alloy by creating a superhydrophobic surface structure through a two-step process of etching followed by polymer modification. *Polymers* **2022**, *14*, 4509. [CrossRef] [PubMed]
4. Prando, D.; Brenna, A.; Diamanti, M.V. Corrosion of titanium: Part 1: Aggressive environments and main forms of degradation. *JABFM* **2017**, *15*, e291–e302. [CrossRef]
5. Zhang, D.; Wei, B.; Wu, Z.; Wang, Z. A comparative study on the corrosion behaviour of Al, Ti, Zr and Hf metallic coatings deposited on AZ91D magnesium alloys. *Surf. Coat. Tech.* **2016**, *303*, 94–102. [CrossRef]
6. Shukla, P.; Awasthi, S.; Ramkumar, J.; Balani, K. Protective trivalent Cr-based electrochemical coatings for gun barrels. *J. Alloys Compd.* **2018**, *768*, 1039–1048. [CrossRef]
7. Marchewka, J.; Kołodziejczyk, E.; Bezkosty, P. Characterization of electrochemical deposition of copper and copper(I) oxide on the carbon nanotubes coated stainless steel substrates. *Sci. Rep.* **2023**, *13*, 6786. [CrossRef]
8. Chen, M.; Liu, D.; Zi, B.; Chen, Y.; Liu, D.; Du, X.; Pan, H. Remarkable synergistic effect in cobalt-iron nitride/alloy nanosheets for robust electrochemical water splitting. *J. Energy Chem.* **2022**, *65*, 405–414. [CrossRef]
9. Wei, B.; Legut, D.; Sun, S.; Wang, H.T.; Shi, Z.Z.; Zhang, H.J.; Zhang, R.F. Synergistic effect of solute and strain on the electrochemical degradation in representative Zn-based and Mg-based alloys. *Corros. Sci.* **2021**, *188*, 109539. [CrossRef]
10. Marinou, A.; Lekatou, A.G.; Xanthopoulou, G.; Vekinis, G. Electrochemical behavior of nickel aluminide coatings produced by CAFSY method in aqueous NaCl solution. *Coatings* **2022**, *12*, 1935. [CrossRef]
11. Wu, P.; Xue, Z.; Yu, T.; Penkov, O.V. Transparent self-cleaning coatings: A review. *Coatings* **2023**, *13*, 1270. [CrossRef]
12. Wang, S.; Wan, Y.; Song, N. Automatically generated datasets: Present and potential self-cleaning coating materials. *Sci. Data* **2024**, *11*, 146. [CrossRef] [PubMed]
13. Zheng, S.; Li, C.; Zhang, Y.; Xiang, T.; Cao, Y.; Li, Q.; Chen, Z. A General strategy towards superhydrophobic self-cleaning and anti-corrosion metallic surfaces: An example with aluminum alloy. *Coatings* **2021**, *11*, 788. [CrossRef]
14. Su, F.; Yao, K. Facile Fabrication of superhydrophobic surface with excellent mechanical abrasion and corrosion resistance on copper substrate by a novel method. *ACS Appl. Mater. Interfaces* **2014**, *6*, 8762–8770. [CrossRef] [PubMed]
15. Kharitonov, D.S.; Kasach, A.A.; Sergievich, D.S.; Wrzesińska, A.; Bobowska, I.; Darowicki, K.; Kurilo, I.I. Ultrasonic-assisted electrodeposition of Cu-Sn-TiO_2 nanocomposite coatings with enhanced antibacterial activity. *Ultrason. Sonochem.* **2021**, *75*, 105593. [CrossRef]
16. Kasach, A.A.; Kharytonau, D.S.; Zharskii, I.M.; Kurilo, I.I. Electrocrystallisation of Cu-Sn-TiO_2 composite coatings in sulphuric acid electrolytes. *Condens. Matter Interphases.* **2022**, *24*, 220–226. [CrossRef]
17. Mitra, D.; Kang, E.-T.; Neoh, K.G. Antimicrobial copper-based materials and coatings: Potential multifaceted biomedical applications. *ACS Appl. Mater. Interfaces* **2020**, *12*, 21159–21182. [CrossRef]
18. Bharadishettar, N.; Bhat, K.U.; Bhat Panemangalore, D. Coating technologies for copper based antimicrobial active surfaces: A perspective review. *Metals* **2021**, *11*, 711. [CrossRef]
19. O'Regan, B.C.; Grätzel, M. A low-cost, high-efficiency solar cell based on dye-sensitized colloidal TiO_2 films. *Nature* **1991**, *353*, 737–740. [CrossRef]
20. Murashkevich, A.N.; Alisienok, O.A.; Zharskii, I.M. Physicochemical and photocatalytic properties of nanosized titanium dioxide deposited on silicon dioxide microspheres. *Kinet. Catal.* **2011**, *52*, 830. [CrossRef]
21. Jain, A.; Vaya, D. Photocatalytic activity of TiO_2 nanomaterial. *J. Chil. Chem. Soc.* **2017**, *62*, 3683–3690. [CrossRef]
22. Mhadhbi, M.; Abderrazak, H.; Avar, B. *Synthesis and Properties of Titanium Dioxide Nanoparticles*; IntechOpen: London, UK, 2023. [CrossRef]

23. Freyre-Fonseca, V.; Téllez-Medina, D.I.; Medina-Reyes, E.I.; Cornejo-Mazón, M.; López-Villegas, E.O.; Alamilla-Beltrán, L.; Gutiérrez-López, G.F. Morphological and physicochemical characterization of agglomerates of titanium dioxide nanoparticles in cell culture media. *J. Nanomater.* **2016**, *2016*, 1–19. [CrossRef]
24. Arumugam, C.; Velu, N.; Radhakrishnan, P.; Roy, V.A.L.; Anantha-Iyengar, G.; Lee, D.-E.; Kannan, V. Studies on the functional properties of titanium dioxide nanoparticles distributed in silyl–alkyl bridged polyaniline-based nanofluids. *Nanomaterials* **2023**, *13*, 2332. [CrossRef] [PubMed]
25. Mehraz, S.; Luo, W.; Swiatowska, J.; Bezzazi, B.; Taleb, A. Hydrothermal synthesis of TiO_2 aggregates and their application as negative electrodes for lithium–ion batteries: The conflicting effects of specific surface and pore size. *Materials* **2021**, *14*, 916. [CrossRef] [PubMed]
26. Praveen, B.M.; Venkatesha, T.V.; Naik, Y.A.; Prashantha, K. Corrosion behavior of Zn-TiO_2 composite coatings. *Synth. React. Inorg. Met. Nano-Met. Chem.* **2007**, *37*, 461–465. [CrossRef]
27. Kang, B.; Lan, D.; Liu, L.; Dang, R.; Yao, C.; Liu, P.; Ma, F.; Qi, S.; Chen, X. Antibacterial activity and bioactivity of Zn-Doped TiO_2 coating for implants. *Coatings* **2022**, *12*, 1264. [CrossRef]
28. Makarava, I.; Esmaeili, M.; Kharytonau, D.S.; Pelcastre, L.; Ryl, J.; Bilesan, M.R.; Vuorinen, E.; Repo, E. Influence of CeO_2 and TiO_2 particles on physicochemical properties of composite nickel coatings electrodeposited at ambient temperature. *Materials* **2022**, *15*, 5550. [CrossRef]
29. Baghery, P.; Farzam, M.; Mousavi, A.B.; Hosseini, M. Ni–TiO_2 nanocomposite coating with high resistance to corrosion and wear. *Surf. Coat. Technol.* **2010**, *204*, 3804–3810. [CrossRef]
30. Thiemig, D.; Bund, A. Characterization of electrodeposited Ni–TiO_2 nanocomposite coatings. *Surf. Coat. Technol.* **2008**, *202*, 2976–2984. [CrossRef]
31. Mozhgan, S.; Mahdi, M.; Seyed, M.E.; Mohammad, A. The role of TiO_2 nanoparticles on the topography and hydrophobicity of electrodeposited Ni–TiO_2 composite coating. *Surf. Topogr. Metrol. Prop.* **2020**, *8*, 025008. [CrossRef]
32. Birlik, I.; Ak Azem, N.F.; Toparli, M.; Celik, E.; Koc Delice, T.; Yildirim, S.; Bardakcioglu, O.; Dikici, T. Preparation and characterization of Ni–TiO_2 nanocomposite coatings produced by electrodeposition Technique. *Front. Mater.* **2016**, *3*, 46. [CrossRef]
33. Rosolymou, E.; Karantonis, A.; Pavlatou, E.A. Effects of direct and pulse plating on the co-deposition of Sn-Ni/TiO_2 composite coatings. *Materials* **2024**, *17*, 392. [CrossRef] [PubMed]
34. Rosolymou, E.; Spanou, S.; Zanella, C.; Tsoukleris, D.S.; Kohler, S.; Leisner, P.; Pavlatou, E.A. Electrodeposition of photocatalytic Sn-Ni matrix composite coatings embedded with doped TiO_2 particles. *Coatings* **2020**, *10*, 775. [CrossRef]
35. Pyanko, A.V.; Makarova, I.V.; Kharitonov, D.S.; Makeeva, I.S.; Sergievich, D.S.; Chernik, A.A. Physicochemical and Biocidal Properties of Nickel–Tin and Nickel–Tin—Titania Coatings. *Prot. Met. Phys. Chem. Surf.* **2021**, *57*, 88–95. [CrossRef]
36. Pyanko, A.V.; Makarova, I.V.; Kharitonov, D.S.; Makeeva, I.S.; Alisienok, O.A.; Chernik, A.A. Tin–Nickel–Titania Composite Coatings. *Inorg. Mater.* **2019**, *55*, 568–575. [CrossRef]
37. Qader, I. Studying the Effect of TiO_2 Coating and Improving Biocompatibility of NiTiSn Biomedical Shape Memory Alloys. Ph.D. Thesis, Fırat University, Elazığ, Turkey, 2021. [CrossRef]
38. Wan, C.; Zhang, L.; Liu, X. Corrosion assessment of Sn-Ni alloy coatings using neutral salt spray tests and electrochemical methods. *Int. J. Electrochem. Sci.* **2020**, *15*, 26–38. [CrossRef]
39. Wan, C.; Liu, X.; Ye, J. Tailorable deposition of Sn-Ni alloy from a pyrophosphate bath with an adjustable Sn:Ni molar ratio. *Surf. Coatings Technol.* **2019**, *369*, 244–251. [CrossRef]
40. Subramanian, B.; Mohan, S.; Jayakrishnan, S. Selective area deposition of tin-nickel alloy-an alternative for decorative chromium plating. *J. Appl. Electrochem.* **2007**, *37*, 219–224. [CrossRef]
41. Lačnjevac, U.; Jović, B.M.; Jović, V.D. Electrodeposition of Ni, Sn and Ni–Sn alloy coatings from pyrophosphate-glycine bath. *J. Electrochem. Soc.* **2012**, *159*, D310–D318. [CrossRef]
42. Rudnik, E. The influence of sulfate ions on the electrodeposition of Ni-Sn alloys from acidic chloride-gluconate baths. *J. Electroanal. Chem.* **2014**, *726*, 97–106. [CrossRef]
43. Jalota, S.K. Tin–nickel alloy plating. *Met. Finish.* **1999**, *97*, 319–322. [CrossRef]
44. Kuznetsov, B.V.; Vorobyova, T.N.; Glibin, V.P. A Comparative study of tin-nickel alloys obtained by electroplating and casting. *Met. Finish.* **2013**, *111*, 38–42. [CrossRef]
45. Lowenheim, F.A.; Sellers, W.W.; Carlin, F.X. The protective value of tin-nickel alloy deposits on steel. *J. Electrochem. Soc.* **1958**, *105*, 338–346. [CrossRef]
46. Shetty, S.; Hegde, A.C. Electrodeposition of Sn-Ni alloy coatings for water-splitting application from alkaline medium. *Metall. Mater. Trans. B.* **2017**, *48*, 632–641. [CrossRef]
47. Refaey, S.A.M.; Taha, F.; Hasanin, T.H.A. Electrochemical behavior of Sn-Ni nanostructured compound in alkaline media and the effect of halide ions. *Appl. Surf. Sci.* **2004**, *227*, 416–428. [CrossRef]
48. Zhu, Y.; Liu, T.; Li, L.; Song, S.; Ding, R. Nickel-based electrodes as catalysts for hydrogen evolution reaction in alkaline media. *Ionics* **2018**, *24*, 1121–1127. [CrossRef]
49. Lačnjevac, U.C.; Jović, V.D.; Jović, B.M. Electrodeposition and characterization of Ni–Sn alloy coatings as cathodematerial for hydrogen evolution reaction in alkaline solutions. *ZAŠTITA Mater.* **2011**, *52*, 153–158.

50. Benea, L.; Danaila, E. Nucleation and growth mechanism of Ni/TiO_2 nanoparticles electro-codeposition. *J. Electrochem. Soc.* **2016**, *163*, D655–D662. [CrossRef]
51. *ISO 27447:2019*; Fine Ceramics (Advanced Ceramics, Advanced Technical Ceramics)—Test Method for Antibacterial Activity of Semiconducting Photocatalytic Materials. ISO: Geneva, Switzerland, 2019.
52. Xue, Y.; Wang, S.; Zhao, G.; Taleb, A.; Jin, Y. Fabrication of NiCo coating by electrochemical deposition with high superhydrophobic properties for corrosion protection. *Surf. Coat. Technol.* **2019**, *363*, 352–361. [CrossRef]
53. Liang, C.; Liu, X.; Teng, F.; Li, Y.; Gao, S. TiO_2/EP superhydrophobic composite coating with excellent mechanical and chemical stability. *Surf. Coat. Technol.* **2024**, *481*, 130641. [CrossRef]
54. Basavegowda, N.; Baek, K.-H. Multimetallic nanoparticles as alternative antimicrobial agents: Challenges and perspectives. *Molecules* **2021**, *26*, 912. [CrossRef] [PubMed]
55. Gold, K.; Slay, B.; Knackstedt, M.; Gaharwar, A.K. Antimicrobial activity of metal and metal-oxide based nanoparticles. *Adv. Therap.* **2018**, *1*, 1700033. [CrossRef]
56. Celardo, I.; Pedersen, J.Z.; Traversa, E.; Ghibelli, L. Pharmacological potential of cerium oxide nanoparticles. *Nanoscale* **2011**, *3*, 1411. [CrossRef] [PubMed]
57. Arreche, R.; Bellotti, N.; Blanco, M.; Vázquez, P. Synthesis and characterization of zirconium oxides for use as antimicrobial additives in paints. *Proc. Mat. Sc.* **2015**, *9*, 627–634. [CrossRef]
58. Nguyen, N.T.; Grelling, N.; Wetteland, C.L.; Rosario, R.; Liu, H. Antimicrobial activities and mechanisms of magnesium oxide nanoparticles (nMgO) against pathogenic bacteria, yeasts, and biofilms. *Sci. Rep.* **2018**, *8*, 16260. [CrossRef] [PubMed]
59. Liu, K.; Cheng, F.; Luo, Y.; Liu, L.; Wang, C.; Xie, K.; Luo, X. Porous single crystalline-like titanium dioxide monolith with enhanced photoelectrochemical performance. *Front. Mater* **2023**, *10*, 1177093. [CrossRef]
60. Alshibeh, A.N.; Vacandio, F.; Vassalo, L.; Djenizian, T.; Coulomb, B.; Boudenne, J.-L. Effects of mode of preparation of titanium dioxide nanotube arrays on their photocatalytic properties: Application to p-nitroaniline degradation. *Micro* **2023**, *3*, 369–381. [CrossRef]
61. Lowry, G.V.; Gregory, K.B.; Apte, S.C.; Lead, J.R. Transformations of nanomaterials in the environment. *Environ. Sci. Technol.* **2012**, *46*, 6893–6899. [CrossRef]
62. Oktar, F.N.; Yetmez, M.; Ficai, D.; Ficai, A.; Dumitru, F.; Pica, A. Molecular mechanism and targets of the antimicrobial activity of metal nanoparticles. *Curr. Top. Med. Chem.* **2015**, *15*, 1583–1588. [CrossRef]
63. Ibáñez, J.A.; Litter, M.I.; Pizarro, R.A. Photocatalytic bactericidal effect of TiO_2 on Enterobacter cloacae. *J. Photochem. Photobiol. A* **2003**, *157*, 81–85. [CrossRef]
64. Wyszogrodzka, G.; Marszalek, B.; Gil, B.; Dorozynski, P. Metal-organic frameworks: Mechanisms of antibacterial action and potential applications. *Drug Discov. Today* **2016**, *21*, 1009–1018. [CrossRef] [PubMed]
65. Abdal Dayem, A.; Hossain, M.; Lee, S.; Kim, K.; Saha, S.; Yang, G.-M.; Cho, S.-G. The role of reactive oxygen species (ROS) in the biological activities of metallic nanoparticles. *Int. J. Mol. Sci.* **2017**, *18*, 120. [CrossRef]
66. Sandulescu, A.; Anastasescu, C.; Papa, F.; Raciulete, M.; Vasile, A.; Spataru, T.; Scarisoreanu, M.; Fleaca, C.; Mihailescu, C.N.; Teodorescu, V.; et al. Advancements on basic working principles of photo-driven oxidative degradation of organic substrates over pristine and noble metal-modified TiO_2. Model case of phenol photo oxidation. *Catalysts* **2021**, *11*, 487. [CrossRef]
67. Laxma Reddy, P.V.; Kavitha, B.; Kumar Reddy, P.A.; Kim, K.-H. TiO_2-based photocatalytic disinfection of microbes in aqueous media: A review. *Environ. Res.* **2017**, *154*, 296–303. [CrossRef] [PubMed]
68. Anandgaonker, P.; Kulkarni, G.; Gaikwad, S.; Rajbhoj, A. Synthesis of TiO_2 nanoparticles by electrochemical method and their antibacterial application. *Arab. J. Chem.* **2015**, *12*, 1815–1822. [CrossRef]
69. Younis, A.B.; Milosavljevic, V.; Fialova, T.; Smerkova, K.; Michalkova, H.; Svec, P.; Antal, P.; Kopel, P.; Adam, V.; Zurek, L.; et al. Synthesis and characterization of TiO_2 nanoparticles combined with geraniol and their synergistic antibacterial activity. *BMC Microbiol.* **2023**, *23*, 207. [CrossRef]
70. Du, T.; Huang, B.; Cao, J.; Li, C.; Jiao, J.; Xiao, Z.; Wei, L.; Ma, J.; Du, X.; Wang, S. Ni nanocrystals supported on graphene oxide: Antibacterial agents for synergistic treatment of bacterial infections. *ACS Omega* **2022**, *7*, 18339–18349. [CrossRef]
71. Yasuyuki, M.; Kunihiro, K.; Kurissery, S.; Kanavillil, N.; Sato, Y.; Kikuchi, Y. Antibacterial properties of nine pure metals: A laboratory study using Staphylococcus aureus and Escherichia coli. *Biofouling* **2010**, *26*, 851–858. [CrossRef]